Materials & Design 212 (2021) 110209

Contents lists available at ScienceDirect

Materials & Design

journal homepage: www.elsevier.com/locate/matdes

Analytical model for predicting residual stresses in abrasive waterjet peening

Zhao Wang [a,b], Zhirong Liao [a,*], Dragos Axinte [a], Xin Dong [a], Dongdong Xu [a], Giedrius Augustinavicius [c]

[a] Machining and Condition Monitoring Group, Faculty of Engineering, University of Nottingham, UK
[b] School of Mechanical Engineering & Automation, Northeastern University, Shenyang 110819, China
[c] Waterjet AG, Switzerland

HIGHLIGHTS

- Theoretical model is proposed for predicting compressive residual stress in abrasive waterjet peening.
- Abrasive sizes, spatial position, and velocity distribution in waterjet beam are considered in prediction model.
- Material work hardening is considered in multiple abrasive overlapping impacts.
- Abrasive distribution on the workpiece depends on the number of peening, traverse speed, and jet centre distance.
- Distribution of compressive residual stress is predicted based on abrasive waterjet peening surface topography.

GRAPHICAL ABSTRACT

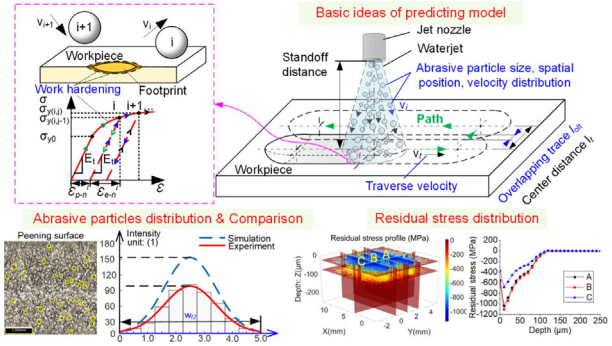

ARTICLE INFO

Article history:
Received 24 June 2021
Revised 7 September 2021
Accepted 27 October 2021
Available online 29 October 2021

Keywords:
Abrasive waterjet peening
Analysis model
Compressive residual stress distribution
Work hardening
Overlapped footprints

ABSTRACT

Abrasive waterjet peening (AWJP) is a new mechanical surface treatment where particles are delivered by a waterjet to induce plastic deformation and achieve surface strengthening effects on a workpiece. Although fatigue strength can be improved by inducing compressive residual stress, the prediction of residual stress distribution remains challenging because particle–workpiece interaction occurs with randomicity, superposition, and overlapping. In this paper, a theoretical model is proposed for predicting workpiece plastic deformation and compressive residual stress by analysing i) the non-uniform energy distribution of the AWJP beam caused by the non-uniformity of the abrasive size, spatial distribution, and impact velocity; ii) material hardening among multiple impacts by abrasive particles; and iii) overlapping traces induced by the changing position of the AWJP beam. The AWJP experiments were conducted in single-pass/multiple-pass/multiple-overlapping footprints with different pump pressures, traverse speeds, and jet centre distances of the adjacent traces to validate the model. The results showed good agreement with the predicted surface roughness and compressive residual stress. Compressive residual stress increased with the pump pressure, whereas the effect of pump pressure change rate decreased when the pump pressure was increased; further, residual stress is nearly constant with the variation in traverse speed and jet centre distance of the adjacent traces when it decreases to a certain value. These results can act as references for the control of residual stress and the prediction model can aid industrial manufacturing in AWJP parameter optimisation (e.g. pump pressure, traverse speed, surface roughness, compressive residual stress, and centre distance between two adjacent traces).

* Corresponding author.
E-mail address: Zhirong.liao@Nottingham.ac.uk (Z. Liao).

https://doi.org/10.1016/j.matdes.2021.110209
0264-1275/

Nomenclature

E_a	Abrasive particle energy (J)
E_{a-p}	Elastic modulus of abrasive particle (Pa)
$E_e^{(i,j)}$	Elastic deformation energy (J)
$E_{e-p}^{(i,j)}$	Energy threshold of workpiece plastic deformation after j th impact(J)
$E_p^{(i,j)}$	Plastic deformation energy of j th impact (J)
E^*	Equivalent elastic modulus
d	Abrasive particle diameter (m)
h_i	Deformation of workpiece at i position
h_w	Thickness of workpiece (m)
i	Random position of workpiece
j	j th abrasive particle of position i
K_t	Material strength index (MPa)
L	Constant (300 MPa)
l_m	Side length of mesh (m) (Figs. 3 and 5)
l_t	Centre distance of two traces (m) (Fig. 5)
m_a	Abrasive particles flow rate (g/min) (Fig. 4)
m_{a-d}	Abrasive mass of each dwell position (g) (Fig. 4)
m_a	Mass of i_a th abrasive particle (g) (Fig. 4)
m_n	Total mass of i_a ($i = n$) abrasive particles (g) (Fig. 4)
N_{a-d}	Number of abrasive particles of each dwell position
n	Constant (0.1368 at 25 °C)
n_t	Strain hardening exponent
P_a	Probability of abrasive particles appearing at a random position
P_i	Equivalent load of i position (N)
P_v	Probability of abrasive particle velocity at a random position
Δp	Pressure drop of inner and outer nozzle (MPa)
R_a	Abrasive radius (m)
r_a	Radial position of abrasive particles (m) (Fig. 2)
r_n	Radius of nozzle (m) (Fig. 2)
s_a	Surface roughness (μm)
s_m	Contact area of each mesh (m^2)
t_{a-d}	Jet nozzle dwell time at each position (s)
v	Abrasive particles mean velocity (m)
v_a	Abrasive velocity at workpiece surface (m/s)
v_t	Jet nozzle traverse speed (mm/min)
v_w	Isentropic velocity of water jet behind orifice (m/s)
x_a	Ratio of abrasive particle radius position and nozzle radius
x_v	Ratio of abrasive particle velocity and isentropic velocity of water jet behind orifice
z_0	Initial surface
σ_b	Workpiece material ultimate tensile stress (MPa)
σ_a, μ_a	Standard deviation and mean value of radial position distribution of the abrasive particles
σ_d, μ_d	Standard deviation and mean value of abrasive particles size
σ_v, μ_v	Standard deviation and mean value of the velocity distribution of abrasive particles
σ_{y_0}	Initial yield stress of workpiece (MPa)
$\sigma_{y_{(i,j)}}$	Yield stress of j th impact (MPa)
α	the ratio of the radius α^p of plastic footprint to elastic contact radius α^e
α_p	Plastic contact radius between abrasive and workpiece (m)
γ_1	Poisson's ratio of abrasive particle
γ_2	Poisson's ratio of Workpiece
$\sum \varepsilon_{(i,j-1)}$	Elastic strain limitation induced by previous deformation
ε_b	Strain corresponding ultimate tensile stress
$\varepsilon_{e_{(i,j-1)}}$	Recoverable elastic strain corresponding energy $E_e^{(i,j)}$
ε_p	Plastic strain
$\varepsilon_{p_{(i,j-1)}}$	Amount plastic strain of previous $j-1$ th impact (Fig. 6)
$\varepsilon_{p_{(i,j)}}$	Plastic strain of j th process (Fig. 6)
$\sum \varepsilon_{p(i,j)}$	Total plastic strain of position i impact by j th abrasive
$\sum \varepsilon_{p(i,N_i)}$	Total plastic strain of position i
ε_{y_0}	Strain limitation of workpiece
ρ	Abrasive particle density (kg/m^3)
ρ_w	Water density (kg/m^3)
ψ	Compressibility coefficient

1. Introduction

Abrasive waterjets (AWJs) gained popularity because of their low processing forces [1], no heat-affected zone [2], high flexibility [3], and no eco-intoxications [4]. The AWJs have been widely applied in material removal and surface treatment (e.g. cutting, milling, drilling, and polishing) of micro and macro components. Abrasive waterjet peening (AWJP) is a new surface treatment process that can be used to induce compressive residual stress on metallic components [5] after other processes [6,7] for enhancing components fatigue strength [8], mechanical strength, corrosion, and wear resistance.

Unlike pure waterjet peening where only water mass and cavitation are employed for surface impingement [9], abrasive particles carried by the waterjet are employed to impinge the workpiece in the AWJP process. This approach of the AWJP process can significantly increase the efficiency of the pump pressure to obtain the desired compressive residual stress when the pump pressure is 140 MPa [10]. This may because abrasive particles, which are considerably harder than water mass and cavitation, can induce extra elastic–plastic deformation (surface topography) on the target material. Compared with conventional shot peening, compressed air is replaced by the waterjet with an additional function of 'cleaning' and 'cooling'. This implies that the waterjet aids in removing abrasive particles/shots and eliminating thermal effects from the surface [11]. Thus, through AWJP, massive compressive residual stress can be added into the workpiece by introducing a significant work hardening effect and without inducing thermal damage or stress concentration caused by embedding abrasive particles. This approach can significantly influence the stress concentration and crack development of the target surface and enhance fatigue strength.

Arola et al. firstly used garnet abrasives to apply AWJP to treat metallic orthopaedic implants (Ti6Al4V) for inducing a rough surface and compressive residual stress [12]. Compressive residual stress induced by pure waterjet peening and AWJP was compared in subsequent research [10] it was found that compressive residual stress with AWJP was higher than twice that of waterjet peening. Further, the effect of abrasive size and pump pressure on surface texture and particle deposition was investigated [11]; the results indicated that a larger abrasive size or pump pressure caused higher surface roughness. However, all of these studies were based on experimental trials, and the formation mechanism and quantitative prediction of residual stress and surface roughness could not be achieved. Sadasivam et al. [5,13] developed a FEM model and studied the elastic prestress effect on the compressive residual stress of AWJP, and found the surface residual stress increased with the workpiece elastic prestress. However, only a single abrasive

particle impact process was modelled in their model, without considering the effect of repeated impacts and overlapping footprints on residual stress distribution; therefore, it is difficult to capture real conditions and explain the mechanisms of AWJP. Zhang et al. [14] established both theoretical and FEM models to study the residual stress field for different target geometrical features of the AWJP process, where the residual stress of the concave surface was found to be larger than that of the convex surface under the same AWJP parameters. However, the abrasive particle size, spatial position, and velocity distribution in the waterjet were not considered, and they are important factors that can affect the plastic deformation of the workpiece surface, surface roughness, and residual stress distribution. Liao et al. conducted research on the surface integrity under a variety of processes [15–17], and surface modification [18] of AWJM where an abrasive waterjet was used to remove the particles embedded in the workpiece. Although residual stress was not modelled, the idea of calculating the general waterjet energy density profile indicates that modelling based on energy distribution is an effective and feasible method.

There are many other studies on compressive residual stress of the shot peening process, wherein the shots are delivered by compressive air. The effect of initial residual stresses on the shot-peened specimen was studied based on a comprehensive experimental and numerical, found that any initial stress field can be wiped out by the shot peening process up to the maximum compressive residual stress point [19]. The microstructure of the workpiece treated by shot peening was measured and analysed [20–23], which provided a good understanding of the residual stress generated mechanism. For the modelling process, compressive residual stress prediction was modelled in Li et al. [24] based on a Hertzian contact theory and approximate elastic–plastic analysis, wherein the peening surface is assumed to be 100% covered. Atluri and Shen [25] studied Li's model and considered shot velocity, they replaced the pre-test parameter with the analytical model. The Ramberg–Osgood model and Ludwick's model were used to modify and calculate the plastic stress and strain in Li's model [26]. Further, this model was applied to predict the peening intensity by Miao et al. [27] it was found that the shot diameter is an important factor influencing the residual stress and fatigue strength. However, few of these models considered the repeated impact process, overlapping footprints, and yield stress increased by the effect of previous shots on residual stress distribution. Sherafatnia et al. [28] considered material hardworking and Coulomb friction between the target surface and shots to improve Li's model. The prediction accuracy was improved by 15% and 8% for different hardening models. However, in this model, the effect of a single abrasive particle is assumed to be suitable for all particles with different sizes and distributions over workpiece surfaces. This assumption neglects uneven surface plastic deformation that affects residual stress distribution particularly when performing AWJP in a local area. Moreover, a model of spherical cavity expansion was proposed by Al-Obaid [29] to predict plastic deformation and residual stress, which improved the adaptability of the modelling process. Fathallah et al. [30] proposed an analytical model of plastic deformation and residual stress distribution by considering the effect of friction and the angle of impingement between the shot and the target; they observed that the residual stress values and equivalent plastic deformation increased in the near-surface region with an increased coefficient of friction. However, the effect of the overlapped footprint and repeated contact between the shot and target on the plastic deformation and distribution of compressive residual stress were not considered in the two models.

Despite the previous studies that focused on the modelling of compressive residual stress, there are still some important factors that can significantly affect the practical stress distribution. To the best of the authors' knowledge, these factors have not been considered (Fig. 1): (i) spatial and velocity distributions of abrasive particles (for AWJP); (ii) overlapped peening footprints; (iii) work hardening in repeat impact; and (iv) spatial distribution of residual stresses. In AWJP, which is a time-dependent process, it is not difficult to observe that the uneven distribution of abrasive particle position and velocity (Fig. 1a) can induce uneven surface topography and compressive residual stress (Fig. 1c), especially in the overlapping position. In addition, because of the discretised contact between the abrasive particles and the workpiece, yield stress varies with a number of impacts (Fig. 1b).

2. Problem definition

This study proposes an analytical model of compressive residual stress distribution in the AWJP process based on energy conservation. The abrasive particle distribution of the abrasive waterjet beam, abrasive-workpiece contact, abrasive particle footprint overlapping process, work hardening between each impact, and compressive residual stress distribution were analysed:

- The energy distribution of the AWJP beam at the jet-workpiece contact surface affects plastic deformation and compressive residual stress. Energy calculation considers the non-uniformity of abrasive particle size, spatial distribution, and impact velocity.
- Influence of jet nozzle traverse speed (v_t) and centre distance (l_t) between adjacent traces (Fig. 1a) on the number of abrasive particles impinging on the workpiece surface. The number variation of abrasive particles is from the footprint that overlaps in single and multiple traces, which reflects the time dependence of AWJP.
- Material hardening is considered by analysing the effects of the previous impact on the material yield stress (Fig. 1b). The yield stress is increased through multiple impingements (Fig. 1b σ_{y0} is increased to $\sigma_{y(i,j-1)}$) when the energy carried by the abrasive particles is beyond the material elastic–plastic critical energy.
- Uneven spatial distribution of compressive residual stress on the AWJP surface (Fig. 1c) is caused by the non-homogeneity of the abrasive particle footprints.

3. Modelling of surface roughness and residual stress in AWJP

The proposed model includes four steps: i) determining the kinetic energy distribution of abrasive particles in the AWJP beam that can influence residual stress spreading (Section 3.1); ii) modelling the abrasive particle–workpiece contact process (Section 3.2), iii) establishing the relationship between abrasive particle kinetic energy and workpiece deformation energy, and determining the workpiece deformation (Section 3.3); and iv) calculating the compressive residual stress (Section 3.4).

The following assumptions were considered to refine the model from practical problems:

- o The water mass does not affect the surface deformation because the water flow energy is largely consumed during the process of sucking abrasive particles, mixing, and accelerating the abrasive particles. Moreover, according to the research of Hashish [31], when the standoff distance is 44 mm with the pump pressure of 310 MPa, there is no obvious peening effect observed in pure water jet impact. The thermal effects are neglected because of the continuous flow of water.

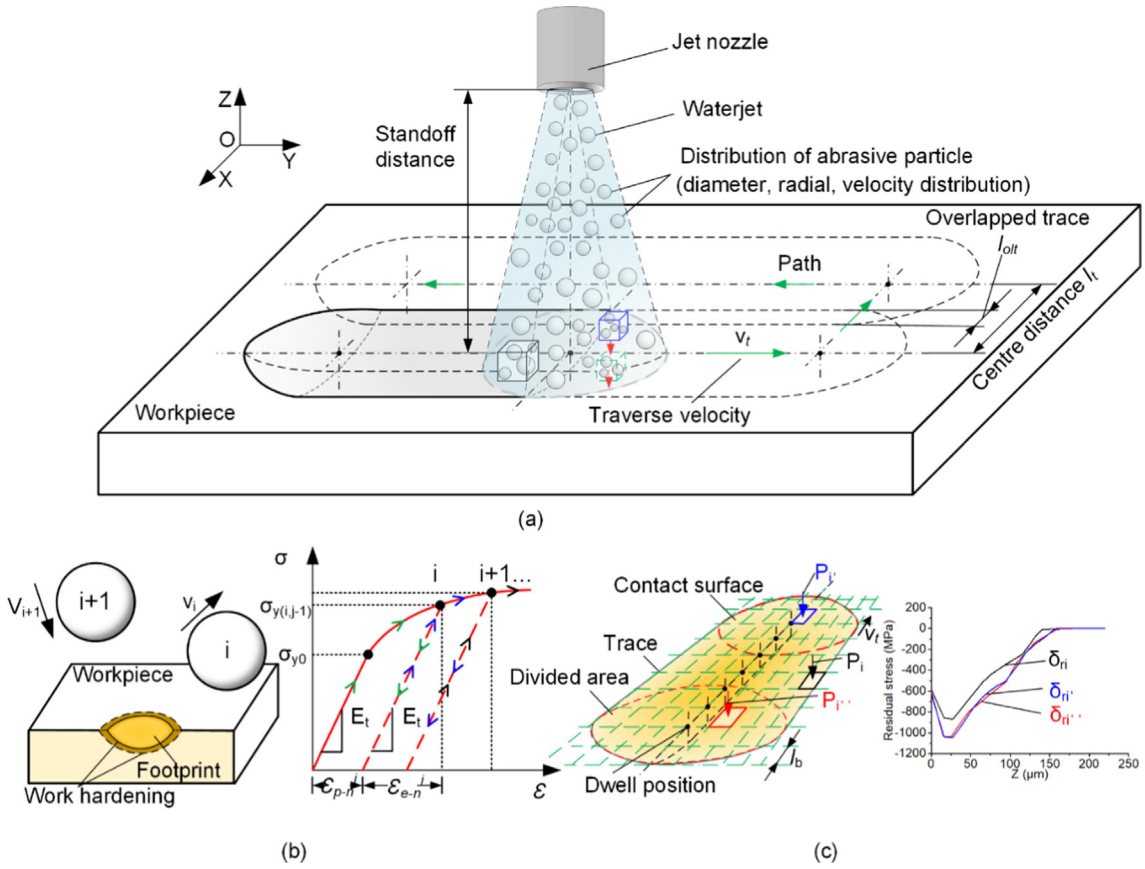

Fig. 1. Schematics of AWJP process: with (a) abrasive particle size, spatial, velocity distribution in waterjet, and overlapped traces; (b) work hardening between two impacted abrasive particles; and (c) distribution of equivalent load and corresponding compressive residual stress.

- Employed peening abrasive particles (i.e. stainless steel balls) are spherical and rigid with no interaction between abrasive particles because of the small abrasive flow rate. All abrasive particles affect the workpiece surface vertically; no fragmentation or embedment of abrasive particles occurs.
- The target workpiece is a semi-infinite body. This is employed for Hertzian contact theory for the compressive residual stress calculation.

3.1. Modelling the kinetic energy of abrasive particles in the AWJP beam

In the AWJP process, abrasive particles spread along a radial direction within the waterjet beam, i.e. high density in the middle zone and less on the edges (Fig. 2) [32]. It is necessary to obtain the distribution of the abrasive particle size, position, and corresponding velocity to obtain the kinetic energy distribution of abrasive particles.

Heiniger [21] and Axinte [33,34] suggested that the spatial distribution of abrasive particles along with the radial position x_a can be assumed to follow a Gaussian distribution, it can be described as

$$P_a(x_a) = \frac{1}{\sqrt{2\pi}\sigma_a} e^{-\frac{(x_a-\mu_a)^2}{2\sigma_a^2}}, \quad (1)$$

where σ_a and μ_a represent the standard deviation and mean value, respectively, P_a represents the probability of x_a, and x_a denotes a dimensionless parameter that can be expressed as

$$x_a = \frac{r_a}{r_n}, \quad (2)$$

where r_a and r_n denote the radial position of the abrasive particle and the radius of the nozzle (Fig. 2), respectively.

According to Heiniger [35] and Lozano [1], the velocity of abrasive particles varies along the radial direction within the AWJP beam similar to its spatial distribution, Gaussian distribution. That is, the ratio of the abrasive particle velocity to the water velocity

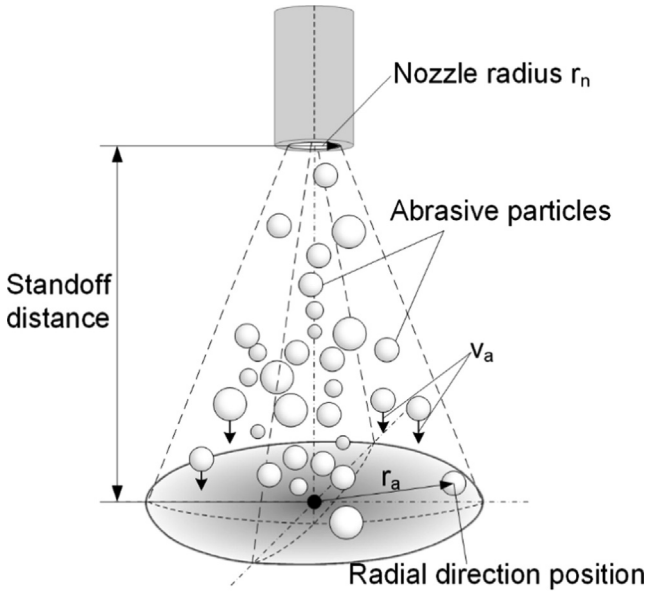

Fig. 2. Schematic of abrasive particles distribution within the waterjet beam.

follows a Gaussian distribution within the AWJP beam. It can be described as

$$P_v(x_v) = \frac{1}{\sqrt{2\pi}\sigma_v} e^{-\frac{(x_v-\mu_v)^2}{2\sigma_v{}^2}}, \tag{3}$$

where σ_v and μ_v represent the standard deviation and mean value, respectively, and P_v denotes the probability of x_v, which is the velocity ratio and is presented as

$$x_v = \frac{v_a}{v_w}, \tag{4}$$

where v_a denotes the abrasive particle velocity and can be calibrated by experiments, and v_w represents the isentropic velocity of the waterjet can be calculated from Bernoulli's function for the momentum balance and water compressibility equation [36], and it can be given by

$$v_w = \psi \cdot \sqrt{\frac{2 \cdot \Delta p}{\rho_w}}, \tag{5}$$

with the mean relative water pressure Δp, water density ρ_w, and compressibility coefficient ψ is described as [35]

$$\psi = \sqrt{\frac{L}{\Delta p \cdot (1-n)} \cdot \left[\left(1 + \frac{\Delta p}{L}\right)^{1-n} - 1\right]}. \tag{6}$$

where constant L is 300 MPa, and constant n equals 0.1368 at 25 °C.

In addition to spatial and velocity distributions, it is necessary to calculate abrasive particle size distribution within the waterjet beam. According to Heiniger [35], abrasive particles with different sizes remain randomly distributed within the AWJP beam. Therefore, the abrasive particle distribution model can be calculated independently.

Diameters (d) of 200 abrasive particles were measured before peening, and the distribution function of the particle size that follows a Gaussian distribution can be described by (Fig. 8e, standard deviation $\sigma_d = 14.65\mu m$, and mean value $\mu_d = 169.76\ \mu m$)

$$F(d) = \frac{1}{\sqrt{2\pi}\sigma_d} e^{-\frac{(d-\mu_d)^2}{2\sigma_d{}^2}}. \tag{7}$$

Thus, the spatial distribution, velocity distribution, and diameter distribution of the abrasive particles were calculated. Then, the kinetic energy of every single abrasive particle (Ea) within the waterjet beam is calculated as

$$E_a = \frac{1}{2}\left(\frac{4}{3}\right)\pi\left(\frac{d}{2}\right)^3 \rho {v_a}^2 = \frac{\pi}{12} d^3 \rho {v_a}^2, \tag{8}$$

with the abrasive particle density ρ.

3.2. Analysis of abrasive particle–workpiece contact process

In this study, the drop-off position of abrasive particles is discretised with $l_m \times l_m$ meshes (Fig. 3a and b) considering the complexity of the abrasive particles overlapping at a jet dwell position and the interaction between abrasive particles and workpiece during continuous jet movement (Fig. 3a). If the dimension of each mesh is sufficiently small, then the abrasive particle footprint can be approximately expressed through a single mesh (Fig. 3 b and c). Thus, the number of abrasive particles drop in the same mesh can be considered to overlap at the same position (Fig. 3 d and e). Consequently, an abrasive particle–workpiece contact condition at each dwell position can be determined. Further, the continuous abrasive waterjet beam moving process can be decomposed into multiple discrete dwell positions (Fig. 3a). If the discrete length of the beam trace l_a is equal to the mesh width l_m (Fig. 3a, b, c), the interaction between the abrasive particle and workpiece during the continuous movement process can be considered as an overlap of meshes. Thus, an abrasive particle–workpiece contact process can be determined analytically.

3.2.1. Abrasive particle–workpiece contact and superposition at dwell position

The number of abrasive particles in each mesh is calculated for analysing the abrasive particle–workpiece contact process. In the first instance, the dimensions of the mesh should be reasonably defined, and then, the abrasive particle mass at a single dwell position is computed to obtain the total number of abrasive particles. Subsequently, the number of abrasive particles in each mesh is determined. Finally, the superposition process of the abrasive particle footprints in each mesh is determined.

The dimensions of the mesh are estimated by the diameter of the abrasive particle footprint (green dashed line in Fig. 3c) to replace the abrasive particle footprint by mesh considering a similar contact area and overlapping process. Miao et al. [27] reported that the relationship between the plastic contact radius α_p of a single particle and the impact velocity v_a can be expressed as

$$\alpha_p = R_a \left(\frac{8\rho {v_a}^2}{9\sigma_{y_0}}\right)^{\frac{1}{4}}, \tag{9}$$

where R_a and v_a are the abrasive particle radius and velocity, respectively, ρ denotes the abrasive particle density, and σ_{y_0} denotes the workpiece yield stress. All meshes are set to the same dimensions as $l_m = 2\alpha_p$ to simplify the calculation process. Here, α_p is calculated by the average abrasive particle radius and velocity.

The total abrasive particle mass at each dwell position can be determined by the abrasive particle flow rate and traverse speed of the waterjet beam; subsequently, the number of abrasive particles can be calculated by its total mass and size distribution function. Assuming the abrasive particle flow rate is m_a, the total abrasive particle mass M_a at a single dwell position can be calculated as

$$M_a = m_a \Delta t, \tag{10}$$

where Δt denotes the dwell time and can be computed using the beam traverse speed v_t and the length of the dwell point (Fig. 3a l_a). The length of the dwell point is kept equal to the dimension of the mesh l_m to simplify the calculation, and therefore, the mass of the abrasive particles at each dwell position is

$$M_a = m_a \frac{l_m}{v_t}. \tag{11}$$

Therefore, as shown in Fig. 4, the number of abrasive particles N_a can be obtained by combining with the abrasive particle size distribution function in Eq. (7), where i_a denotes the number of abrasive particles, M_{i-a} denotes the mass of the $i_a th$ abrasive particle, and M_n denotes the total mass of i_a abrasive particles.

The mesh size, positions, abrasive particle number, and velocity in each mesh can be determined (Fig. 3) based on the distribution function (spatial position, velocity, and size) presented in Section 3.1. Further, the impact process of abrasive particles in each mesh can be regarded as an orderly impact process (Fig. 3e) considering the independent act between abrasive particles and the workpiece in the actual condition and the work hardening phenomenon. The abrasive particle–workpiece contact surfaces of different dwell positions can be considered as the overlapping process of meshes.

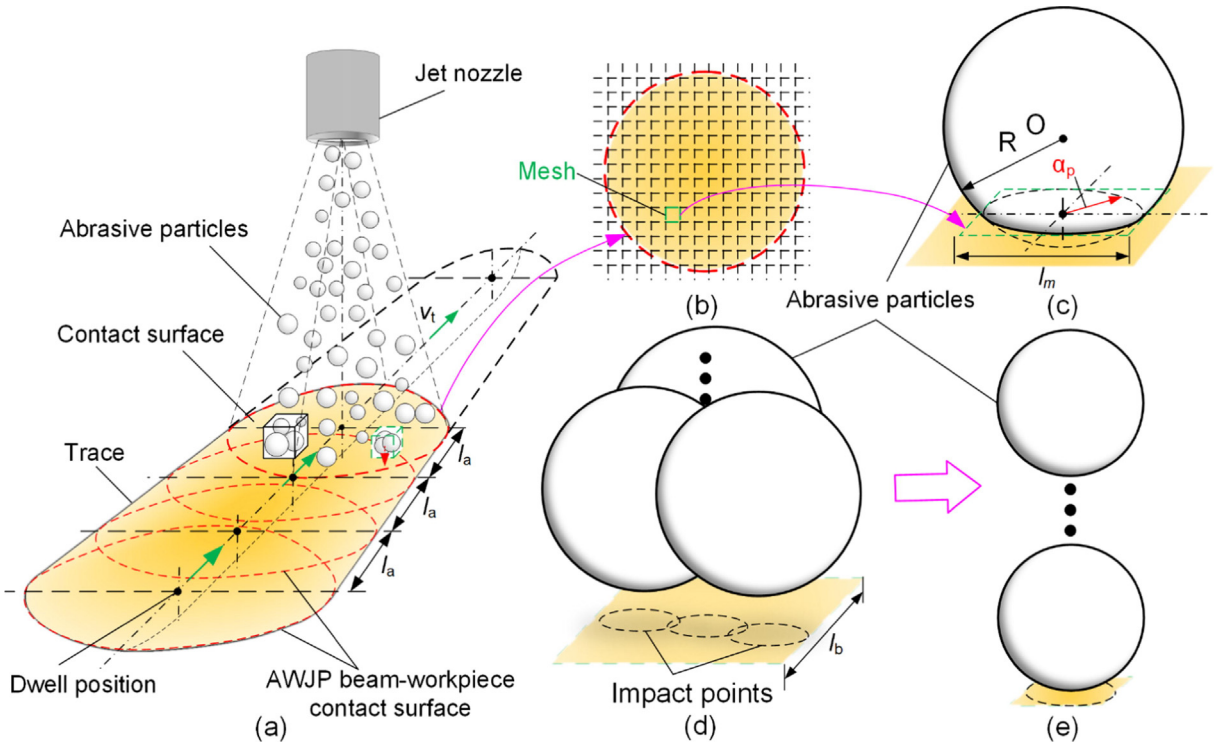

Fig. 3. Schematics of abrasive particle–workpiece contact and superposition process. (a) Peening process of a single trace, (b) division of contact area between abrasive waterjet beam and workpiece at dwell position, (c) mesh size setting process, (d) number of abrasive particles in each mesh, and (e) overlapping approximation of abrasive particles impact within the same mesh.

3.2.2. Abrasive particles superposition of single trace and overlapping traces

It is necessary to analyse the abrasive particle–workpiece contact and superposition process in peening traces to allow the modelling of the entire surface peening process after determining the contact and superposition between the abrasive particles and workpiece at a single dwell position.

Superposition at the trace level contains two cases: Superposition in the i) single trace counting from the waterjet beam movement and ii) between adjacent traces depending on the trace centre distance (Fig. 5a, l_t).

To simplify the process, these two cases are analysed together (Fig. 5a) because they can both be considered the partial overlapping of the dwell position. The centre distance of two adjacent traces is set as l_t. Further, the trace centre distance l_t can be divided into multiple segments depending on the dimension of the mesh l_m because the dimension of the mesh l_m is sufficiently small. Thus, the overlapping traces can be analysed by overlapping the footprints of each mesh.

The random footprint ($mesh_0$) of trace i was selected to analyse the overlapping process (Fig. 5a) to facilitate understanding. The abrasive particles of mesh1, mesh2, and mesh3 overlap on the mesh0 position in sequence at times t_1, t_2, and t_3, respectively, when the AWJP beam moves along trace ii, as shown in Fig. 5b. The abrasive particles of each mesh acting process were analysed, as shown in Fig. 3d and e.

3.3. Energy conversion and surface roughness

The kinetic energy of a single abrasive particle and the distribution and superposition of the particles can be obtained based on the above discussion. The next step is to determine the relationship between the kinetic energy of the abrasive particles and workpiece deformation.

3.3.1. Constitutive model and work hardening

In AWJP, abrasive particles affect the workpiece one after another and follow different stress–strain relations (Green and blue arrows in Fig. 6a). This is because the stress–strain model at the local position can be influenced by the previous impact/work hardening effect. This implies that the yield stress at different workpiece positions varies with impact history. According to Ludwik's equation [37], the constitutive model of materials at locally impacted position can be expressed as

$$\sigma = \sigma_{y_0} + K_t \varepsilon_p^{n_t}, \tag{12}$$

where σ, σ_{y_0}, ε_p, K_t, and n_t denote the stress, initial yield stress, plastic strain, material strength index, and strain hardening exponent, respectively.

Assuming that the material at mesh i is subjected to j-1 times impacting deformation, the yield stress is increased by a factor depending on the amount of plastic strain $\sum \varepsilon_{p_{(i,j-1)}}$. Hence, the stress–strain relation in the next impact (j times) can be expressed as

$$\sigma_{y(i,j)} = \sigma_{y_0} + K_t\left(\sum \varepsilon_{p(i,j-1)} + \varepsilon_{p(i,j)}\right)^{n_t}. \tag{13}$$

where $\varepsilon_{p_{(i,j)}}$ denotes the plastic strain by the j^{th} impact.

3.3.2. Relationship between energy and plastic deformation

In the abrasive particle–workpiece contact process, energy carried by the abrasive particle varies with the abrasive particle size, position, and velocity. That is, not all abrasive particles have sufficient energy to generate deformation on the workpiece surface. Therefore, the workpiece deformation energy threshold varies with each mesh because of the effect of the previous impact deformation. Further, the plastic deformation energy threshold of the different impact times is determined to calculate the plastic deformation.

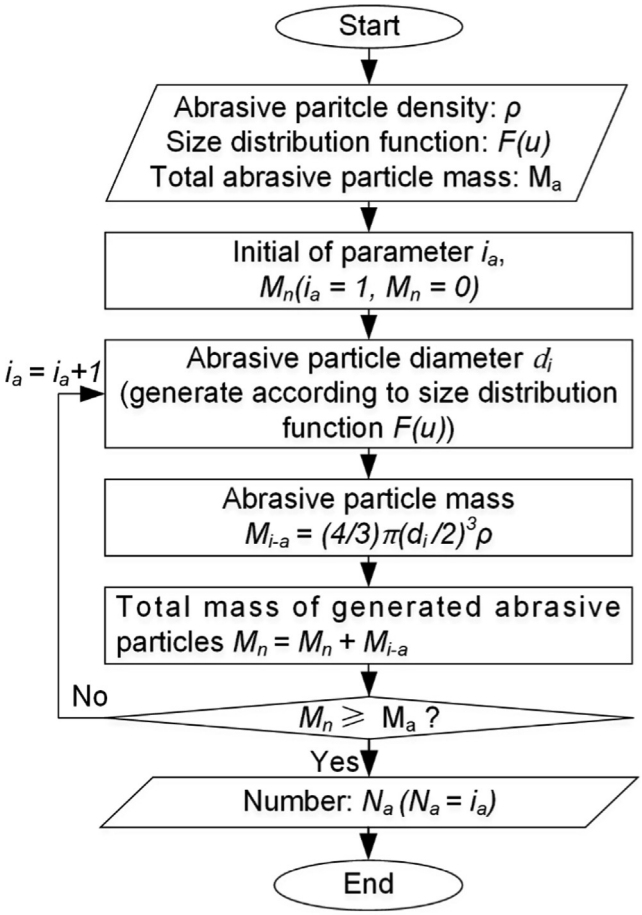

Fig. 4. Schematic of the calculation of abrasive particle number at each dwell position.

The impact of the j[th] abrasive particle at mesh position i is selected to facilitate understanding. Considering prior impact deformation $\sum \varepsilon_{p_{(i,j-1)}}$ according to the energy conservation law and the constitutive model in Eq. (13), the workpiece elastic–plastic transformation energy threshold ${E_{e-p}}^{(i,j)}$ (Fig. 6b) of the jth impact can be calculated as

$$ {E_{e-p}}^{(i,j)} = s_m h_w \int_0^{\varepsilon_{y_{(i,j-1)}}} E_t \varepsilon_y d\varepsilon = \frac{1}{2}\sigma_{y_{(i,j-1)}} \varepsilon_{y_{(i,j-1)}} s_m h_w, \tag{14} $$

where s_m, h_w, E_t, ε_y denote the mesh contact area at position i, thickness of workpiece, elastic modulus, and yield strain induced by the previous deformation and updated by $\varepsilon_{y_{(i,j-1)}}$, respectively, which is equal to

$$ \varepsilon_{y_{(i,j-1)}} = \frac{\sigma_{y_{(i,j-1)}}}{E_t} = \frac{\sigma_{y_0} + K_t \sum \varepsilon_{p(i,j-1)}^{\,n_t}}{E_t}. \tag{15} $$

${E_{e-p}}^{(i,j)}$ can be considered the initial energy threshold used to set up the processing parameter when $\sum \varepsilon_{p(i,j-1)}$ $(j = 1,\ \sum \varepsilon_{p(i,0)} = 0)$. Because the peening process aims to introduce residual stress on the original surface, the stress $\sigma_{y_{(i,j-1)}}$ and yield strain $\sum \varepsilon_{p_{(i,j-1)}}$ in Eq. (15) are replaced by the workpiece initial yield stresses σ_{y_0} and 0, respectively.

Therefore, when an abrasive particle (energy E_a, Eq. (8)) interacts with the workpiece, two different cases occur:

Case (i): Abrasive particle kinetic energy ${E_a}^{(i,j)}$ (Equation (8)) is smaller than the workpiece plastic deformation threshold energy ${E_{e-p}}^{(i,j)}$ Eq. (14).

According to the law of conservation of energy and Hook's law,

$$ {E_a}^{(i,j)} = {E_e}^{(i,j)} = s_m h_w \int_0^{\varepsilon_{e_{(i,j-1)}}} E_t \varepsilon_{e(i,j-1)} d\varepsilon, (\varepsilon_{e_{(i,j-1)}} \le \varepsilon_{y_{(i,j-1)}}) \tag{16} $$

where ${E_a}^{(i,j)}$ denotes the abrasive particle kinetic energy, and ${E_e}^{(i,j)}$ and $\varepsilon_{e_{(i,j-1)}}$ are the elastic deformation energy and recoverable elastic strain corresponding energy ${E_e}^{(i,j)}$, respectively.

In this case, the constitutive model (Fig. 6) is unchanged and can be used for the next contact process because no plastic strain occurs.

Case (ii): Abrasive particle kinetic energy ${E_a}^{(i,j)}$ is larger than the workpiece elastic–plastic critical deformation threshold energy ${E_{e-p}}^{(i,j)}$.

Abrasive particle kinetic energy ${E_a}^{(i,j)}$ can be decomposed into the maximum elastic–plastic critical deformation energy ${E_{e-p}}^{(i,j)}$ (energy threshold) and the plastic deformation energy ${E_p}^{(i,j)}$

$$ {E_a}^{(i,j)} = {E_{e-p}}^{(i,j)} + {E_p}^{(i,j)}, \tag{17} $$

where ${E_{e-p}}^{(i,j)}$ can be calculated using Eq. (14), and ${E_p}^{(i,j)}$ can be expressed by Eq. (18) according to the energy conservation law and the constitutive model in Eq. (13).

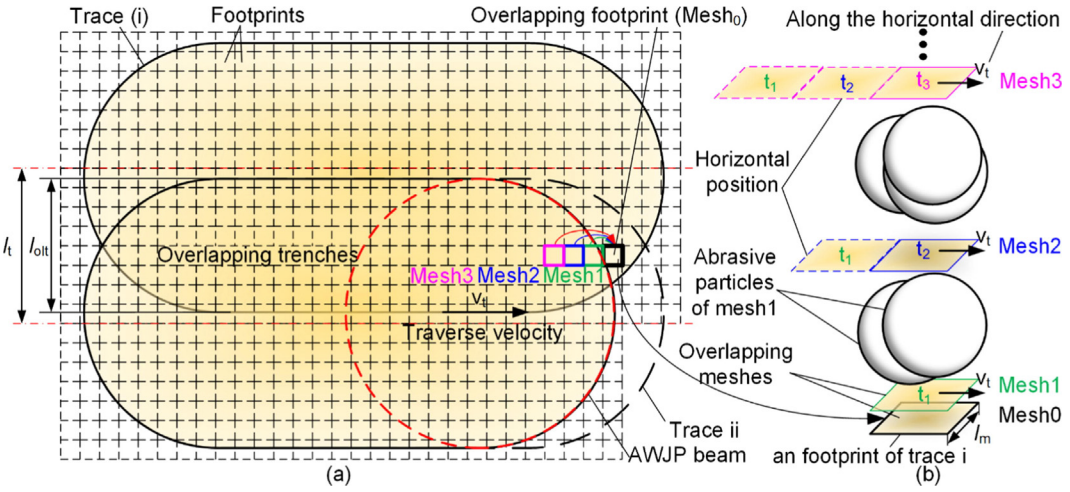

Fig. 5. Schematics of footprint superposition analysis process of traces with overlapping process of (a) two adjacent traces and (b) meshes (jet beam at different dwell position).

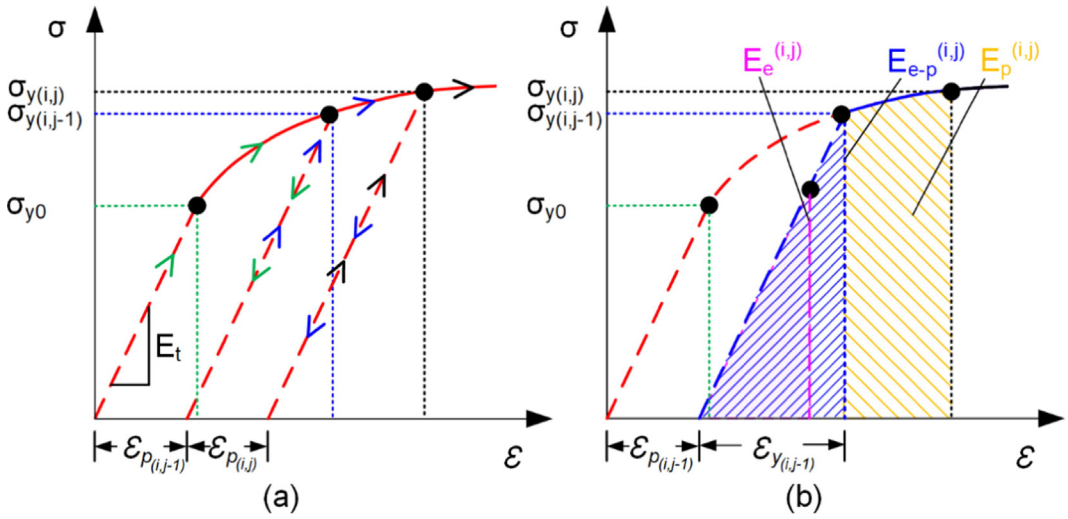

Fig. 6. Schematics of (a) constitutive relation and (b) deformation energy.

$$E_p^{(i,j)} = s_m h_w \int_{\varepsilon_{y_{(i,j-1)}}}^{\varepsilon_{y_{(i,j-1)}}+\varepsilon_{p_{(i,j)}}} \left(\sigma_{y_0} + K_t\left(\sum \varepsilon_{p_{(i,j-1)}} + \varepsilon_{p(i,j)}\right)^{n_t}\right) d\varepsilon, \tag{18}$$

where $\sum \varepsilon_{p(i,j-1)}$ denotes the prior plastic strain from Eq. (15), and $\varepsilon_{p(i,j)}$ denotes the incremental plastic strain corresponding to the energy $E_a^{(i,j)}$, which can be calculated. The total plastic strain caused by all $\sum j (j = 1, 2, \ldots, j, \ldots, N_i)$ abrasive particles in the same mesh i can be described as

$$\sum \varepsilon_{p(i,j)} = \sum \varepsilon_{p(i,j-1)} + \varepsilon_{p(i,j)}, \tag{19}$$

Consequently, the total strain $\sum \varepsilon_{p(i,N_i)}$ of mesh i can be computed when the total number N_i is determined.

In this case, the constitutive model is updated because of the updating plastic deformation and yield stress $\sigma_{y_{(i,j)}}$ (Fig. 6), the constitutive model can be described as

$$\begin{cases} \sigma_{y_{(i,j)}} = \sigma_{y_0} + K_t\left(\sum \varepsilon_{p(i,j)}\right)^{n_t} \\ \sigma_{y_{(i,j+1)}} = \sigma_{y_0} + K_t\left(\sum \varepsilon_{p_{(i,j)}} + \varepsilon_{p_{(i,j+1)}}\right)^{n_t} \end{cases}, \tag{20}$$

where $\varepsilon_{p_{(i,j+1)}}$ denotes the plastic strain of the $(j+1)^{\text{th}}$ impact $(j = 1, 2, \ldots, j, \ldots, N_i)$.

3.3.3. Surface roughness

According to the total strain $\sum \varepsilon_{p_{(i,N_i)}}$, the total deformation of mesh i induced by the impact of all N_i abrasive particles can be calculated as

$$h_i = h_w \sum \varepsilon_{p_{(i,N_i)}}, \tag{21}$$

The final topography z_{fin} of the machined surface can be predicted using Eq. (22) if the deformation h_i $(i = 1, 2, \ldots, n)$ of all mesh N_m are obtained.

$$z_{fin} = z_0 - h_i, \tag{22}$$

with the initial surface topography z_0.

Furthermore, surface roughness [38,39] can be expressed as

$$S_a = \frac{1}{A} \iint_A |z_{fin}(x, y)| dxdy, \tag{23}$$

where A denotes the area, $z_{fin}(x, y)$ denotes the corresponding depth, and (x, y) denotes the plane position.

3.4. Calculation of compressive residual stress

Residual stress is the internal stress distribution locked into the material; these stresses were present even after the external loading forces were removed. They are a result of the material obtaining equilibrium after it has undergone plastic deformation [40]. Although the AWJP is a continuous impact process, only the final state is meaningful in the industry. Therefore, the final state of the surface topography was used to analyse the compressive residual stress.

In this study, the compressive residual stress was calculated based on [24–28]. According to [24–28] (a more detailed derivation is given in the Appendix), assuming that the peening surface is 100% covered, it can have a relationship between the load and compressive residual stress as

$$\sigma_r = f_{p-\sigma}(\boldsymbol{P}, \boldsymbol{d}, \rho, E^*, K_t, n_t, z). \tag{24}$$

where P denotes the contact load between the abrasive particles and workpiece; d denotes the diameter of the abrasive particle (here, mean value); and $\rho, E^*, K_t,$ and n_t are the material properties of the abrasive particle and workpiece.

Here, 100% coverage is only accepted for each small mesh as the number of abrasive particles in the adjacent mesh is similar; and small area is easily covered. In this case, the contact load in Eq. (24) can be replaced by equivalent load P_i (Fig. 7a and the corresponding residual stress in Fig. 7b) based on the constitutive model; the plastic strain $\varepsilon_{p(i,N_i)}$ of mesh i can be calculated as

$$P_i = \left(\sigma_{y_0} + K_t\left(\sum \varepsilon_{p_{(i,N_i)}}\right)^{n_t}\right) h_w s_m. \tag{25}$$

where $\sum \varepsilon_{p_{(i,N_i)}}$ denotes the amount of plastic strain at point i after the N_i^{th} abrasive particle, which can be calculated using Eq. (19).

4. Experimental methodology

A series of AWJP trials was performed to validate the derived model. The surface roughness, and compressive residual stress were measured and compared with those calculated using the proposed model.

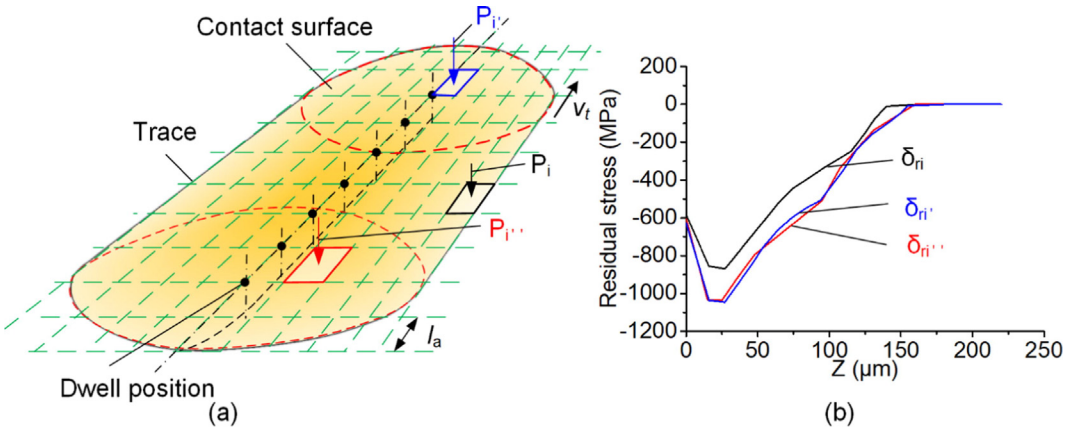

Fig. 7. Schematics of (a) equivalent load distribution and (b) corresponding residual stress.

4.1. Setup and materials parameters

AWJP (Fig. 8a) was conducted on an Inconel 718 plate with abrasive particles (commercial stainless steel shots AMACAST ES-140, with average diameter of 160 μm, the size distribution has been remeasured and counted). The initial surface roughness of the workpiece (Inconel 718) was $Sa = 7.70$ μm. The workpiece was heat treated (500 °C for 2.5 h, air cooling) to eliminate the residual stress from previous processes as much as possible. The initial surface residual stress was measured to be −79.3 ± 43.1 MPa. The properties of Inconel 718 at 25 °C are listed in Table 1 [41–43]. Before running the experiments, the abrasive particle size (Fig. 8d) and initial workpiece surface topography were measured using an optical 3D surface profiler (Alicona G4, see Fig. 8b). The particle size distribution is shown in Fig. 8e. After the experiments, the Inconel 718 plate was divided into several parts with different dimensions of 60*30*8, 60*40*8 mm, and for each part has 3 or 4 footprints with length 50 mm. The peening surfaces were measured by Alicona G4 and PROTO i-XRD, see Fig. 8(b) and (c) for surface roughness and compressive residual stresses, respectively.

In AWJP, the orifice diameter is 0.18 mm and the nozzle diameter is 0.5 mm. Other related parameters are listed in Table 2 for evaluating different analysis factors (Table 3).

4.2. Determination of spatial and velocity distributions of abrasive particles

The footprints on the workpiece were used to calculate the spatial and velocity distribution functions of the abrasive particle. According to [35], abrasive particles with different sizes remain randomly distributed within the AWJP beam; the velocity distribution of the abrasive particles is considered to be uniform. Only the footprint position is required and collected to fit the spatial distribution function in the abrasive particle radial distribution statistical process. In the statistical velocity distribution, only the footprint radius and depth are required to obtain the velocity distribution function.

The footprints were measured in the case of #11 and used for the particle spatial and velocity distribution determination in all cases in Table 2. This is because the variable pump pressure has almost no effect on the abrasive particle radius position-nozzle

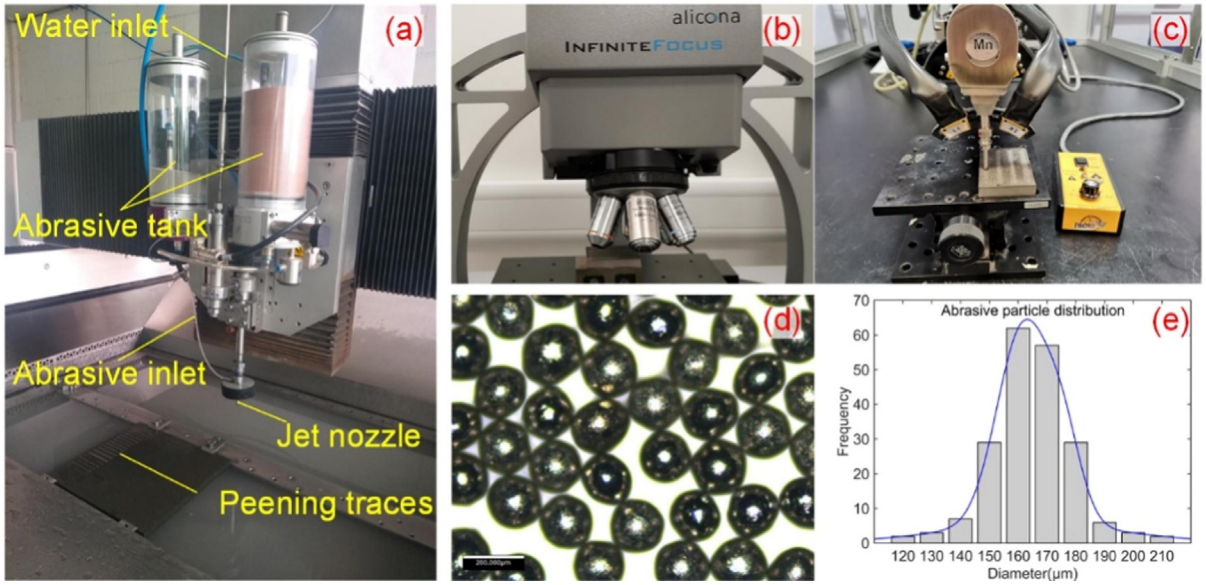

Fig. 8. Schematics of AWJP setup, measurement system, abrasive particles and size distribution, with (a) experimental process, (b) surface topography measure process, (c) residual stress measure process, (d) abrasive particles, and (e) abrasive particle size distribution.

Table 1
Workpiece properties.

Elastic modulus E_t (Gpa)	Yield stress $\sigma_{y_0}(MPa)$	Strength index $k_t(MPa)$	Strain hardening exponent n_t	Poisson ratio γ_2
200	505.8	1472.2	0.4	0.284

Table 2
Parameters used in AWJP experiments.

No.	Pump pressure (MPa)	Traverse speed(mm/min)	Jet centre distance (mm)	Abrasive flow rate (g/min)	Stand-off distance (mm)
#0	100	300	0 (once)	12	40
#1	200	300	0 (once)	12	40
#2	300	300	0 (once)	12	40
#3	200	100	0 (once)	12	40
#4	200	200	0 (once)	12	40
#5	200	200	0 (twice)	12	40
#6	200	200	0 (four times)	12	40
#7	200	300	0 (Three times)	12	40
#8	200	200	1 (two traces)	12	40
#9	200	200	2 (two traces)	12	40
#10	200	200	3 (two traces)	12	40
#11	200	1000	0 (once)	12	40

Table 3
Analysis elements and corresponding experiments.

Analysis No.	Analysis factor	Experiment No.
# A1	Pump pressure (100, 200, 300 *MPa*)	#0, #1, #2,
# A2	Traverse speed (100, 200,300,1000 mm/min)	#3, #4, #1, #11
# A3	The number of peening (once, twice, four times)	#4, #5, #6,
# A4	The number of peening (with the same total abrasive mass, through changing the traverse speed)	#3, #5, #7,
# A5	Jet centre distance 1, 2, 3 mm	#8, #9, #10

radius ratio x_a and the abrasive-water velocity ratio x_v when the standoff distance and abrasive flow rate are determined [35]. #11 was selected to obtain clear and relatively sparse footprints at a high traverse speed (1000 mm/min).

The radial positions of the footprints were collected (Image J software, Fig. 9a), and the abrasive particle–workpiece contact depth and contact radius of the footprints were collected (Mountain map software) as shown in Fig. 9b and c.

According to the radial position of the 200 abrasive particles, the mean value of the abrasive particle radius position-nozzle radius ratio and the standard deviation can be calculated as $\mu_a = -0.069$ and $\sigma_a = 1.916$. The distribution function is described as

$$P_a(x_a) = \frac{1}{1.916 * \sqrt{2\pi}} e^{-\frac{(x_a+0.069)^2}{2*1.916^2}}. \tag{26}$$

Similarly, according to the footprint depth λ and contact radius α_p, the abrasive particle radius R_a (see Fig. 10) can be approximately computed as

$$R_a = \frac{\alpha_p{}^2 + \lambda^2}{2\lambda}. \tag{27}$$

According to Eq. (9), the abrasive particle velocity can be calculated as

$$v_a = \frac{3\sqrt{\sigma_{y0}}(\alpha_p/R_a)^2}{2\sqrt{2\rho}}. \tag{28}$$

The abrasive particle–water velocity ratio x_v can be obtained by combining the abrasive particle velocity Eq. (28) with the water velocity in Eq. (5). The average value and standard deviation can be calculated as $\mu_v = 0.18$ and $\sigma_v = 0.07$, respectively. The distribution function in Eq. (3) can be determined as

$$P_v(x_v) = \frac{1}{0.07\sqrt{2\pi}} e^{-\frac{(x_v-0.18)^2}{2(0.07)^2}}. \tag{29}$$

5. Results and discussion

5.1. Verification for abrasive particle distribution

The footprints of AWJP are used to validate the abrasive particle distribution. Fig. 11 shows the AWJP footprints at traverse speeds of 300 and 1000 mm/min. As expected, the footprint intensity of the traverse speed of 300 mm/min was significantly larger than

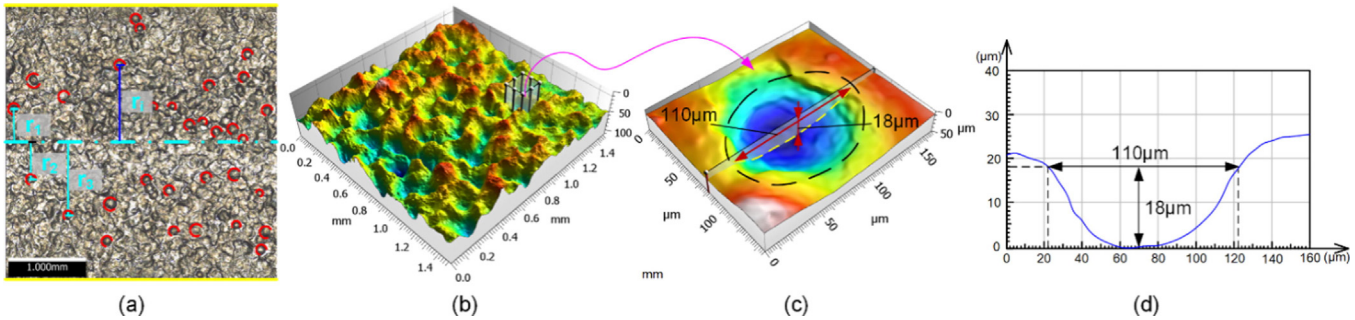

Fig. 9. Schematics of data collection process. (a) experimental surface topography with pump pressure 200 MPa, abrasive flow rate 12 g/min, traverse speed 1000 mm/min, (b) 3D graph of mountain map software at dwell position, (c, d) measurement of footprint depth with 3D and 2D topography, respectively.

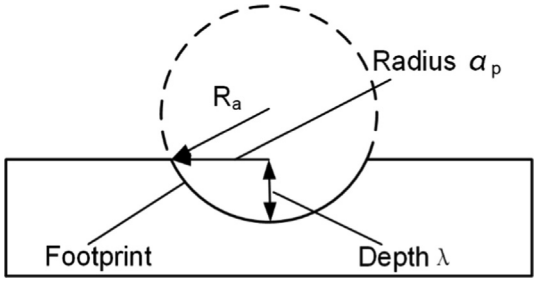

Fig. 10. Schematics of the abrasive particle radius calculated process.

that at 1000 mm/min (Fig. 11a1 and a2). Both show that the footprint distribution intensity of the centre position is larger than that of the edge position (Fig. 11b1, b2, c1, and c2); further, the intensity of the footprint gradually decreases from the centre to the edges, as shown in Fig. 11(a1) and (a2). The width w_{t1} of the footprints in Fig. 11a1 and c1 is larger than the width w_{t2} in Fig. 11a2 and c2, which indicates the probability of abrasive particle footprints distributed at the edge is increased because of the increased number of abrasive particles caused by the reduced traverse speed. This can indicate the normal distribution of the abrasive particles.

Further, footprint intensity was collected and fitted from the experiment (red rectangle, width 2 mm, in Fig. 11 a1 and a2); it was found that the footprint distribution from the centre to the edges follows a Gaussian distribution (red line in Fig. 11d1 and d2). This is similar to the calculated abrasive particle distribution based on the modelling (blue dashed line in Fig. 11d1 and d2). Fig. 11(d1) and (d2) show that the abrasive particle intensity distributed at the centre position is larger than the corresponding footprint intensity; however, the intensity of the abrasive particles at the position of the edge shows good agreement with the corresponding footprints. This is because the overlapping footprints are increased when the traverse speed is reduced from 1000 mm/min to 300 mm/min (Fig. 11(b1) and (b2)), which makes the counted footprint less than the actual footprints. However, there are fewer abrasive particle footprints at the edge, and few overlapping footprints occur when the traverse speed decreases (Fig. 11c1 and c2). This indicates the accuracy of the Gaussian distribution function parameters.

5.2. Verification for abrasive-water velocity ratio x_v, Eq. (4) and Eq. (29)

Footprints under jet pressures of 100 and 300 MPa are shown in Fig. 12 a1 and a2, respectively. A total of 20 independent footprints are extracted in Fig. 12b1 and b2; the depth of the footprints increases with jet essure. This is because the kinetic energy of the abrasive particles increases with the jet pressure, which causes an increase in workpiece deformation.

The depth and diameter of the 20 footprints under jet pressures of 100 MPa and 300 MPa were measured; the mean value is indicated by the red line in Fig. 12c1 and c2. Compared with the calculated footprints of a single abrasive particle with a diameter of 169.76 μm (mean abrasive diameter), the jet pressures of 100 MPa and 300 MPa (the blue dashed line in Fig. 12c1 and c2) are calculated based on the average abrasive-water velocity ratio $x_v = 0.18$, which was obtained using the jet pressure of 200 MPa (Equation (29) in Section 4.2). The measured and calculated results are in good agreement, which proves that ratio x_v is almost unchanged with the jet pressure and can be used to establish the relationship between the jet pressure and abrasive particle kinetic energy.

5.3. Verification for surface roughness

A short trace length (2.5 mm) in Fig. 13a, which was selected for surface roughness calculation, was referenced to the standard length of surface roughness (Ra = 2–10 μm). The surface roughness (Sa) is a square area (2.5 × 2.5 mm) aligned with the trace centreline (Fig. 13b).

The comparison of surface roughness with respect to jet pressure (#0–#2 in Table 4) indicated that surface roughness increased

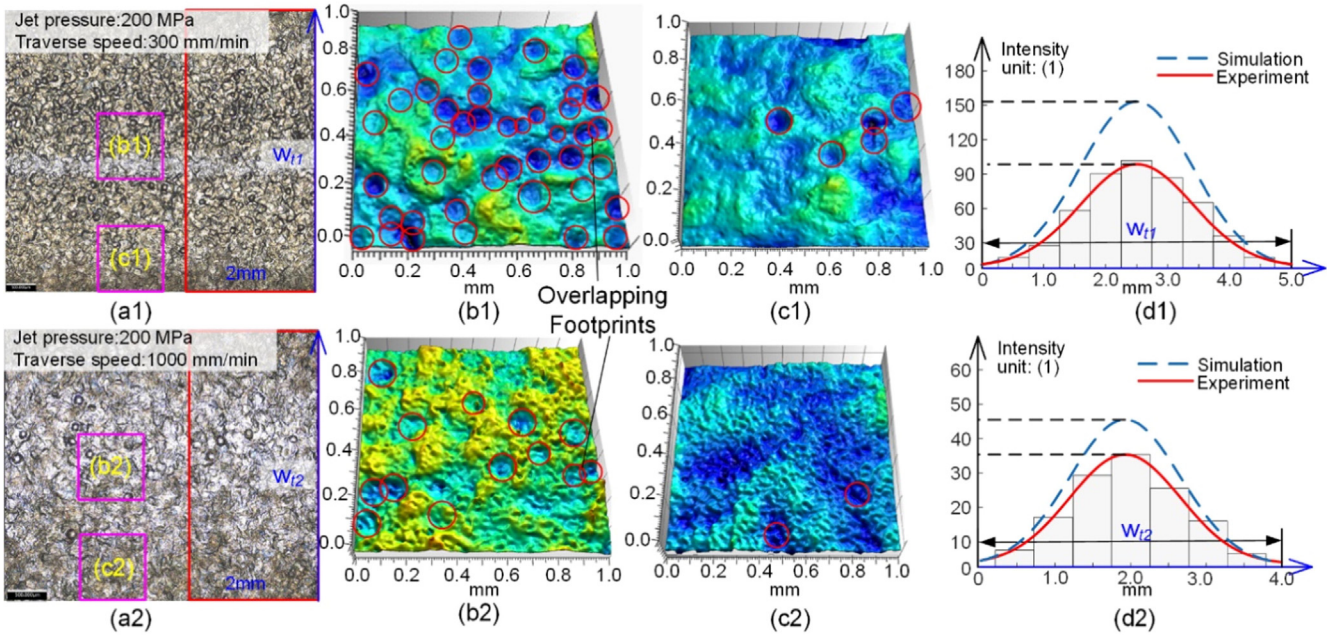

Fig. 11. Schematics of abrasive particle footprints distribution. (a1, a2) Experimental footprint distribution with jet pressure 200 MPa, traverse speeds = 1000 mm/min and 300 mm/min, respectively. (b1, b2, c1, and c2) footprint distributions of the centre and edge positions of (a1) and (a2), respectively. (d1, d2) Comparison of experimental footprint intensity and simulating abrasive particle distribution.

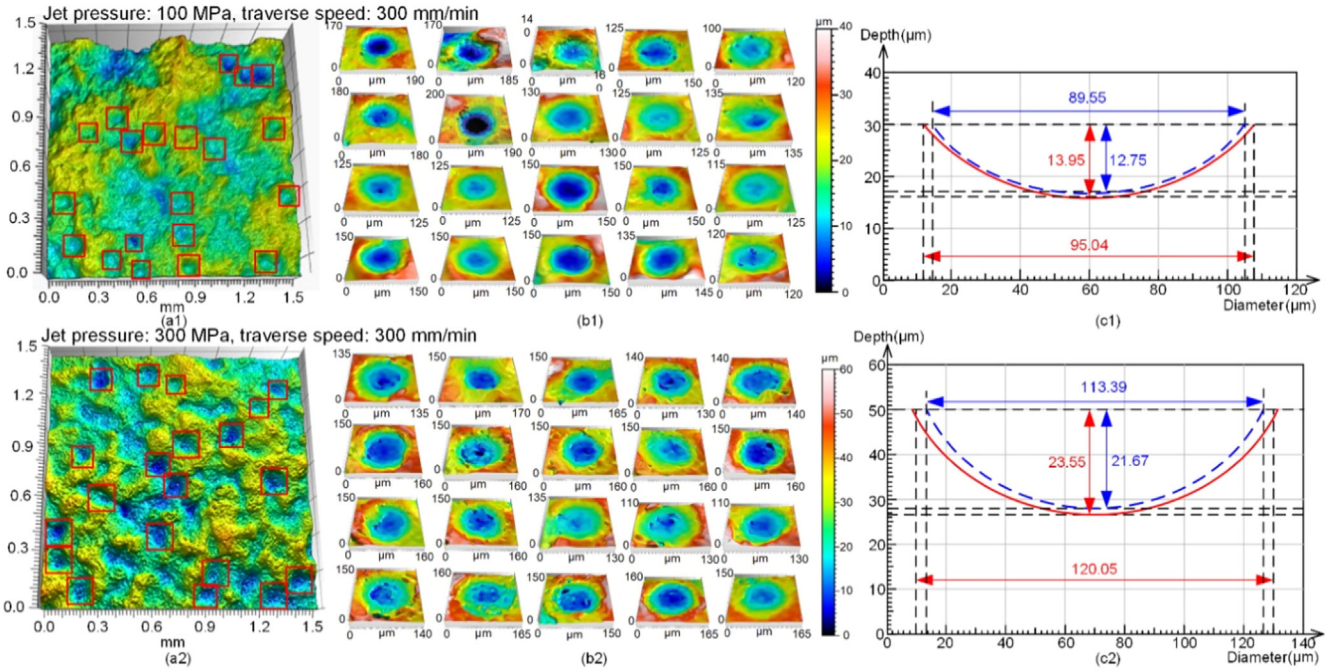

Fig. 12. Schematics of footprints of multiple abrasive particles and a single abrasive particle footprint. (a1, a2) Experimental footprint with traverse speed 300 mm/min and jet pressures of 100 and 300 MPa, respectively, (b1, b2) abrasive particle footprint of special position in (a1) and (a2), (c1, c2) mean footprints depth and abrasive-workpiece contact diameter of 20 abrasive particles footprints in (b1) and (b2) and the corresponding calculated values according to the modelling.

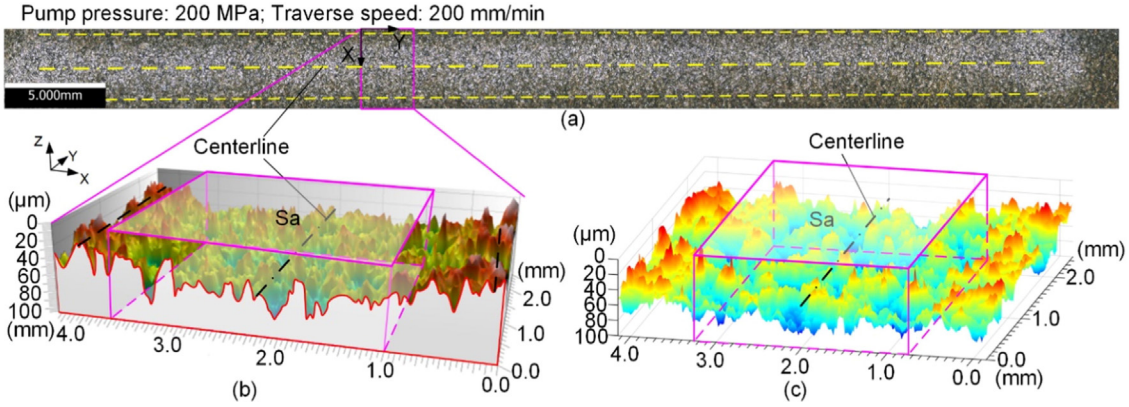

Fig. 13. Comparison of experimental and calculated surface roughness. (a) AWJP surface with jet pressure 200 MPa, traverse speed 200 MPa, (b) extracted area for measuring surface roughness, and (c) corresponding calculation surface roughness.

Table 4
Comparison of surface roughness under different AWJP pump pressure, traverse speed, and jet centre distance.

No.	Pump pressure (MPa)	Traverse speed (mm/min)	Jet centre distance (mm)	Simulation surface roughness (μm)	Experiment surface roughness (μm)	Error
#0	100	300	0 (1 pass)	8.72	7.91	10.2%
#1	200	300	0 (1 pass)	9.39	8.71	7.8%
#2	300	300	0 (1 pass)	10.4	9.56	8.8%
#3	200	100	0 (1 pass)	9.23	8.44	9.4%
#4	200	200	0 (1 pass)	9.29	8.61	7.9%
#5	200	200	0 (2 passes)	9.31	8.32	11.2%
#6	200	200	0 (4 passes)	9.27	8.79	5.5%
#7	200	300	0 (3 passes)	9.33	8.27	12.8%
#8	200	200	1 (2 traces)	9.15	8.57	6.8%
#9	200	200	2 (2 traces)	9.20	8.45	8.9%
#10	200	200	3 (2 traces)	8.90	8.59	3.6%
#11	200	1000	0 (1 pass)	9.05	8.02	12.8%

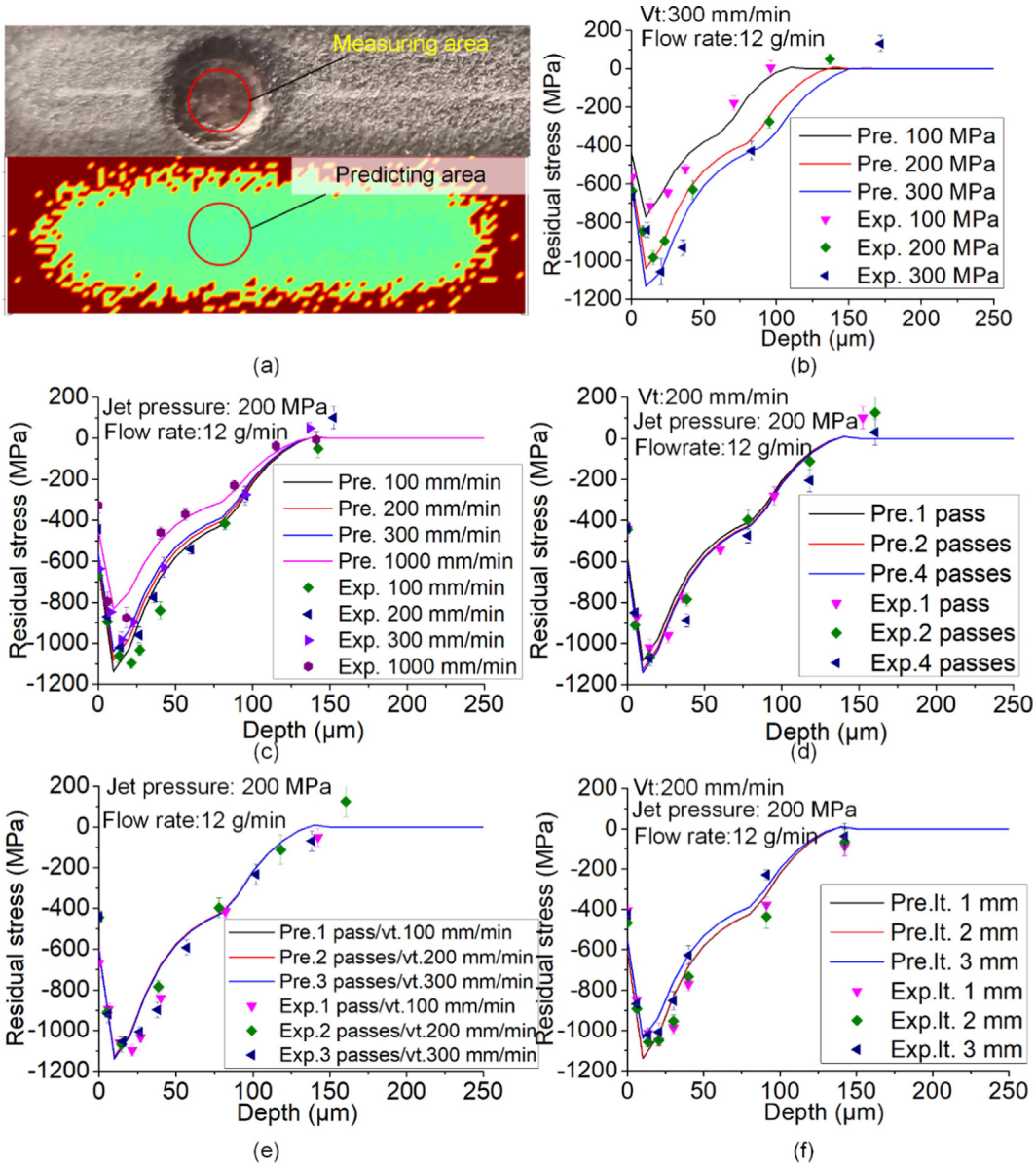

Fig. 14. Schematics of predicting and experimental compressive residual stress with different peening parameters. a) measured and predicted area, b) compressive residual stress with jet pressures of 100, 200, and 300 MPa, c) compressive residual stress with jet nozzle traverse speeds of 100, 200, 300, and 1000 mm/min, d) and e) number of passes (with the same and different total abrasive particle mass) influence on residual stress, and f) residual stress with the jet centre distances of 1, 2, and 3 mm.

at a high jet pressure because of the increased non-uniformity from the higher particle carried energy. The predicted surface roughness is slightly higher than the experimental value ($Sa_{Pre.}$ and $Sa_{Exp.}$ in Fig. 13) because the square mesh is used to instead of the spherical mesh when modelling the abrasive particle–workpiece contact process. However, all results show that the maximum prediction error is 12.8% and the minimum error is 3.6%, which proves the accuracy of the model to a large extent. Further, the predicted surface roughness in the proposed model is calculated based on the initial surface roughness $Sa = 7.70$. The scanned initial surfaces were meshed and updated by the footprints from the abrasive particles.

5.4. Verification for predicting residual stress

The prediction model was validated in terms of (i) comparison of the predicted and experimental residual stresses, and (ii) residual stress distribution according to the proposed model.

5.4.1. Comparison of the predicting and experimental residual stress

The experimental compressive residual stress was measured in a circular area with a diameter of 2 mm (Fig. 14a). The residual stress variation in depth was measured using electro etching in this area. The same circular area coinciding with the trace centreline (Fig. 14a) was selected to calculate the average predicted residual stress for validating the modelling result.

- Compressive residual stress variation trend

The prediction results indicate the same compressive residual stress variation trend as the experimental results (see solid lines and spots in Fig. 14). With an increase in the jet pressure, the compressive residual stress in depth increased, and the thickness of the compressive residual stress layer also increased (Fig. 14b). Abrasive particles with high kinetic energy supply a higher external force on the workpiece, which result in a larger plastic deformation layer. In this case, the workpiece needs to generate a higher internal stress, i.e. compressive residual stress, in a deeper position.

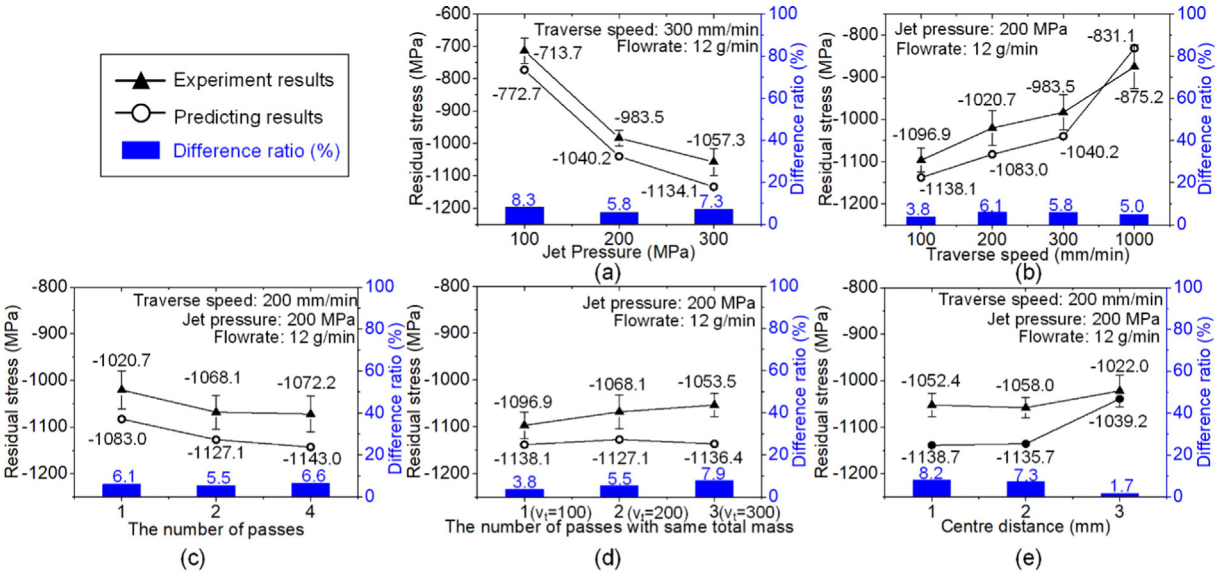

Fig. 15. Comparison of predicting and experimental maximum compressive residual stresses, and the varying trend of the maximum compressive residual stress with different peening parameters. a) Jet pressure, b) traverse speed, c) number of peening with different abrasive mass, d) number of peening with the same abrasive mass, and e) centre distance effect on compressive residual stress.

The compressive residual stress increases with a decrease in the traverse speed (from 1000 mm/min to 100 mm/min); the thickness of the compressive residual stress layer is almost unchanged (Fig. 14c). However, when the traverse speed was from 300 mm/min to 100 mm/min, there was no significant difference in the residual stress because abrasive particles are distributed in a sparse manner for 1000 mm/min, which results in an incomplete coverage (<100% cover). When the traverse speed was reduced to 300 mm/min, with more abrasive particles compressing, the workpiece surface was well covered. The workpiece is further covered by continuing to reduce the speed; a lower increase occurs in the stress and stress layers. This can be verified by increasing the number of peening. At a 200 mm/min traverse speed, the compressive residual stress does not change during repeat peening (Fig. 14d). In other words, when the total mass of the abrasive particles is fixed and set above a critical value, peening while changing the traverse speed and peening number barely affected the stress (Fig. 14e). These observations are consistent with those of previous studies [44,45].

During the peening of the entire surface by multiple trace generation, the coverage was determined by the centre distance. This can be observed by measuring the compressive residual stress in the overlapping position between the two adjacent traces. This implies the stress in such a position decreases as the centre distance increases beyond a certain limit (Fig. 14f).

- Maximum compressive residual stress

The maximum compressive residual stress under the above conditions was collected to better specify the differences between the prediction and experiment. All 12 sets of comparison results indicate that the maximum error is 8.3%; the minimal error is only 1.7% (Fig. 15).

Further, the maximum stress could better indicate the changing rate under different conditions. The rate of increase decreased as the jet pressure increased (Fig. 15a, from 37.8% to 7.5% for the experiments). When the traverse speed was below 300 mm/min, it was nearly fully covered, and the changing rates under different conditions were less than 7% (Fig. 15b-e).

5.4.2. Compressive residual stress distribution

In contrast to the local measurement of residual stress in the experiment, our model can predict the compressive residual stress distribution over the entire peening surface. Here, we select case #10 (jet pressure = 200 MPa, traverse speed = 200 mm/min, centre distance = 3 mm, and flow rate = 12 g/min). Different cross-sections of the peening two traces were selected to better observe the 3D distribution of the residual stress (Fig. 16a). In the top view (cross-section i) of the generated traces, the compressive residual stress map outline (yellow dashed line in Fig. 16c) is consistent with the footprint outline (yellow dashed line in Fig. 16b). The left view (cross-section iii in Fig. 16d) and front view (cross-section ii in Fig. 16e) indicates that the compressive residual stress is not well distributed near the trace overlapping and edge. The stress is shown in Fig. 16f for the three positions at the trace overlapping, centreline, and edge.

Stress distribution shows consistency (the maximum compressive residual stress and stress layer thickness) when the abrasive particle coverage over the workpiece surface is saturated under the same peening condition. However, the edge of the trace has less coverage saturation and smaller compressive residual stress. If the edge is fully covered, then the coverage around the trace centre will be supersaturated, which will lead to time wastage and incur external costs. When peening the entire surface with multiple traces overlapping, the control of trace centre distance is meant to increase the particle coverage near the overlapping (i.e. edges of two adjacent traces) with minimal cost.

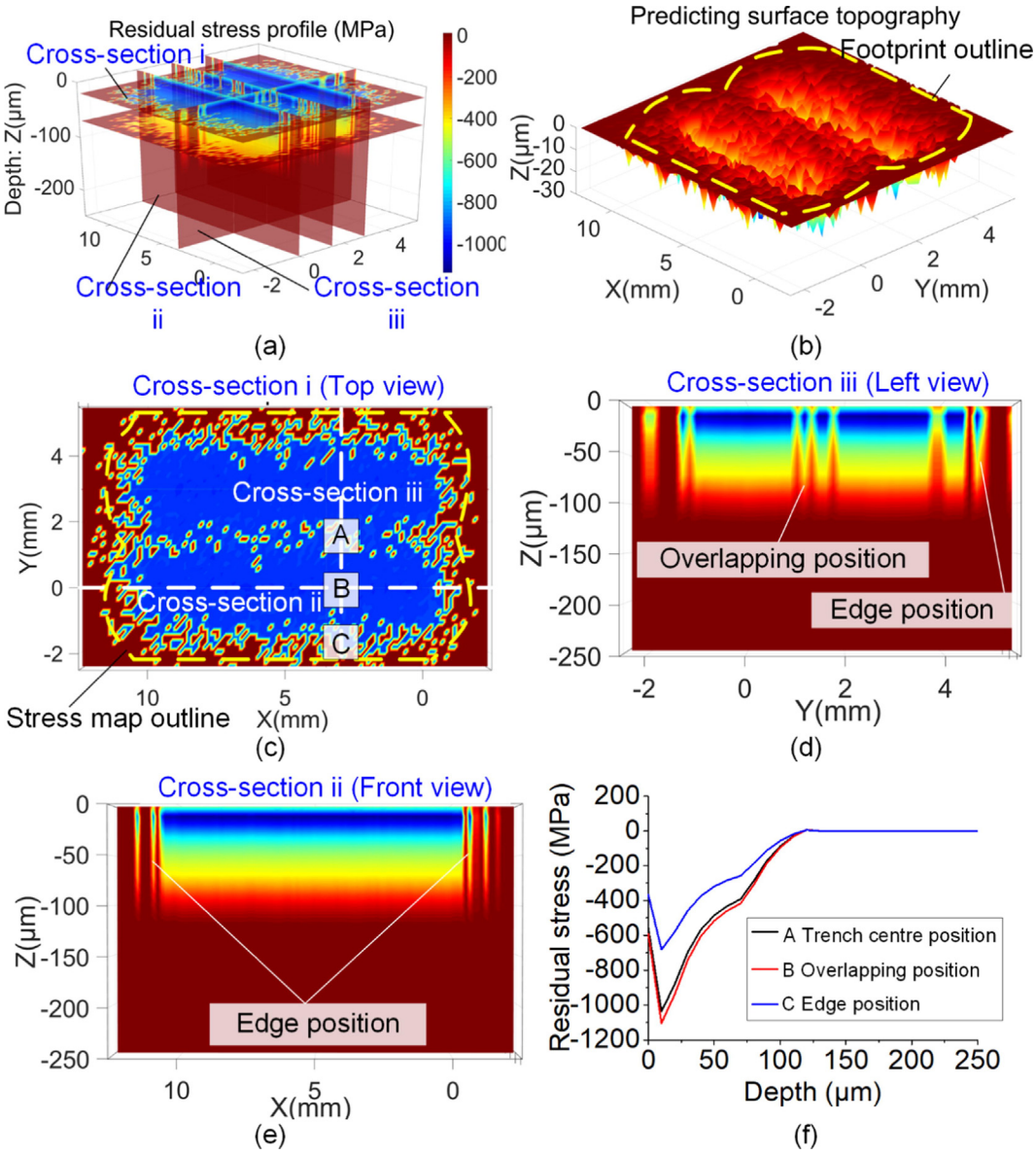

Fig. 16. Residual stress distribution according to the model with the 3D surface topography of #10 experiment with parameters (jet pressure = 200 MP, traverse speed = 200 mm/min, centre distance = 3 mm, abrasive particle flow rate = 12 g/min, stand-off distance = 40 mm). (a) 3D distribution of compressive residual stress, (b) corresponding surface topography, (c, d, e) top, left, and front views of the residual stress distribution, respectively, and (f) residual stress of areas A, B, and C of (c).

6. Conclusion

This paper proposes a mathematical model for predicting the surface roughness and compressive residual stress distribution in AWJPs. The energy distribution of the abrasive particles is considered to be dependent on abrasive particle size, spatial position, and velocity distribution. During AWJP, such energy is partially transformed into the workpiece, which results in plastic deformation on the workpiece surface and further implanting compressive residual stress. Workpiece material hardening is considered among the multiple abrasive–workpiece contact process. The key conclusions of this study are as follows.

1. Surface roughness predicted by the model agrees well with the experimental results; all 12 sets of relative errors of quantitative comparisons are less than 15%, which validates that the proposed model enables the prediction of surface roughness.
2. The model was validated by comparing the predicted and experimental compressive residual stresses of the AWJP surface centre position. All 12 sets of comparison results show that the maximum error is 8.3%; the minimal error is only 1.7%. Further, the proposed model first allows the prediction of compressive residual stress for a specific position and distribution on an entire peening surface.
3. Both experimental and calculated results prove that the considerations in the model may be necessary. These considerations include (i) abrasive particle size, spatial position, and velocity distribution; (ii) material work hardening; (iii) overlapping footprints of both abrasive particle footprints and overlapping traces; and (iv) the number of passes, traverse speed, and centre distance of the abrasive waterjet beam.
4. Based on the model and experiments confirm that the AWJP process with higher jet pressure can implant a larger residual stress while trading off surface accuracy. The compressive

residual stress increases with the jet pressure, while the effect of the jet pressure change rate slows down when the jet pressure is increased.

Declaration of Competing Interest

The authors declare the following financial interests/personal relationships which may be considered as potential competing interests: [Mr. Zhao Wang (The University of Nottingham, UK; Northeastern University, China). Dr. Zhirong Liao (The University of Nottingham, UK). Prof. Dragos Axinte (The University of Nottingham, UK). Dr. Xin Dong (The University of Nottingham, UK). Dr. Dongdong Xu (The University of Nottingham, UK). Dr. Giedrius Augustinavicius (Waterjet AG, Switzerland)].

Acknowledgement

This study was supported by EPSRC through the NanoPrime initiative (EPSRC Reference: EP/R025282/1). The first author also gratefully appreciates the financial support provided by the China Scholarship Council.

Appendix A. The compressive residual stress calculation process

The solutions process of compressive residual stress according to the abrasive particles and workpiece contact load P, and abrasive particle diameter d were provided based on research of [24–28].

A.1. Stress–strain analysis of elastic contact

According to Hertz contact theory [24], the principal stress along x, y and z directions can be expressed by

$$\begin{cases} {\sigma_x}^e = {\sigma_y}^e = -q_0\left(\frac{1}{2}A + (1+\gamma_2)B\right) \\ {\sigma_z}^e = -q_0 A \end{cases} \tag{A1}$$

where q_0 is the maximum Hertz contact force, can be calculated through the contact load P

$$q_0 = \left(\frac{6PE^{*2}}{\pi^3 R^2}\right)^{\frac{1}{3}} \tag{A2}$$

with abrasive particle radius $R = d/2$, E^* is the equivalent elastic modulus, described as

$$E^* = \frac{1-{\gamma_1}^2}{E_1} + \frac{1-{\gamma_2}^2}{E_2} \tag{A3}$$

$E_{1,2}$ and $\gamma_{1,2}$ are the elastic modulus and Poisson's ratio of the abrasive particle and the workpiece, respectively. A and B are geometric parameters, expressed as

$$\begin{cases} A = \left(1 + \left(\frac{z}{a_e}\right)^2\right)^{-1} \\ B = 1 - \left(\frac{z}{a_e}\right) tan^{-1}\left(\frac{a_e}{z}\right) \end{cases} \tag{A4}$$

where z is the depth of the predicted point in the workpiece, and a_e is the elastic contact radius of the abrasive particle-workpiece, expressed as

$$a_e = \left(\frac{3PR}{4E^{*2}}\right)^{\frac{1}{3}}. \tag{A5}$$

Furthermore, the Von-Mises equivalent stress ${\sigma_i}^e$ [24], based on the calculated principal stresses ${\sigma_x}^e$, ${\sigma_y}^e$ and ${\sigma_z}^e$, can be expressed as

$${\sigma_i}^e = \sqrt{\frac{\left({\sigma_x}^e - {\sigma_y}^e\right)^2 + \left({\sigma_y}^e - {\sigma_z}^e\right)^2 + \left({\sigma_z}^e - {\sigma_x}^e\right)^2}{2}} \tag{A6}$$

According to Hooke's law [26], the main strain in the target material can be expressed as:

$$\begin{cases} \varepsilon_x = \varepsilon_y = \frac{1}{E_2}\left[{\sigma_x}^e - \gamma_2\left({\sigma_y}^e + {\sigma_z}^e\right)\right] \\ \varepsilon_z = \frac{1}{E_2}\left({\sigma_z}^e - 2\gamma_2{\sigma_x}^e\right) \end{cases} \tag{A7}$$

The equivalent strain corresponding stress can be expressed as

$${\varepsilon_i}^e = \frac{{\sigma_i}^e}{E_2} \tag{A8}$$

Further, the hydrostatic stress and strain can be expressed as [25]

$${\sigma_m}^e = \frac{1}{3}\left({\sigma_x}^e + {\sigma_y}^e + {\sigma_z}^e\right), \tag{A9}$$

$${\varepsilon_m}^e = \frac{1}{3}\left(\varepsilon_x + \varepsilon_y + \varepsilon_z\right). \tag{A10}$$

The stress deflection tensor of the target material can be expressed as [27]

$$\begin{cases} s_x^e = s_y^e = {\sigma_x}^e - {\sigma_m}^e = \frac{1}{3}{\sigma_i}^e \\ s_z^e = {\sigma_z}^e - {\sigma_m}^e = -\frac{2}{3}{\sigma_i}^e = -2s_x^e \end{cases}. \tag{A11}$$

Strain deflection tensor can be expressed as

$$\begin{cases} e_x^e = e_y^e = \frac{1}{3}(1+\gamma_2){\varepsilon_i}^e \\ e_z^e = -\frac{2}{3}(1+\gamma_2){\varepsilon_i}^e = -2e_x^e \end{cases}. \tag{A12}$$

A.2. Elastic-plastic analysis of the loading process

Elastic-plastic deformation occurs, when the contact load P further increases and the equivalent stress ${\sigma_i}^e$ is greater than the yield stress σ_y of the workpiece. Here, a simplified method of Li et al. [24] is used to calculate the strain field to obtain the stress–strain deflection tensor. Assuming that the plastic strain in the elastic–plastic deformation stage is obtained from the strain field generated by pure elastic impact and the characteristics of complete plastic impact, a coefficient α is introduced to establish the relationship between plastic strain and elastic strain, then the strain in the loading process can be

$${\varepsilon_i}^p = \begin{cases} {\varepsilon_i}^e & {\varepsilon_i}^e \le \varepsilon_{y_0} \\ \varepsilon_{y_0} + \alpha({\varepsilon_i}^e - \varepsilon_{y_0}) & \varepsilon_{y_0} < {\varepsilon_i}^e \end{cases}, \tag{A13}$$

where ε_{y_0} is the strain corresponding to the yield stress σ_y, coefficient α is the ratio of the maximum abrasive particle-workpiece plastic indentation radius α_p to the maximum elastic indentation radius α_e

$$\alpha = \frac{\alpha_p}{\alpha_e} \tag{A14}$$

in which the elastic contact radius α_e can be obtained by Eq. (A5), the plastic contact radius α_p can be obtained by Miao et al. [27]

$$\alpha_p = R\left(\frac{8\rho\nu^2}{9\sigma_{y_0}}\right)^{\frac{1}{4}}. \tag{A15}$$

According to the elastic–plastic stress–strain relationship, as shown in Fig. A1, the stress during the loading process can be expressed as

$$\sigma_i^p = \begin{cases} \sigma_i^e, & \varepsilon_i^p < \varepsilon_{y_0} \\ \sigma_{y_0} + H\left(\varepsilon_i^p - \varepsilon_{y_0}\right), & \varepsilon_{y_0} \le \varepsilon_i^p < \varepsilon_b \\ \sigma_b, & \varepsilon_b \le \varepsilon_i^p \end{cases} \tag{A16}$$

where H is the linear strain hardening index, and σ_b is the ultimate tensile stress of the workpiece.

To obtain the stress deflection tensor, the strain deflection tensor should be obtained first. Based on the analysis process of the elastic loading process, the strain deviation in the elastic–plastic loading stage can be expressed as

$$\begin{cases} e_x^p = e_y^p = \frac{1}{3}(1+\gamma_2)\varepsilon_i^p \\ e_z^p = -\frac{2}{3}(1+\gamma_2)\varepsilon_i^p = -2e_x^p \end{cases}. \tag{A17}$$

According to the elastic–plastic theory of Ilyushin et al. [25–27], the stress deflection tensor in the elastoplastic loading stage can be expressed as

$$\begin{cases} s_x^p = s_y^p = \frac{1}{1+\gamma_2}\frac{\sigma_i^p}{\varepsilon_i^p}e_x^p = \frac{1}{3}\sigma_i^p \\ s_z^p = -\frac{2}{3}\sigma_i^p = -2s_x^p \end{cases} \tag{A18}$$

A.3. Calculation of residual stress after unloading

According to Atluri et al.[26], it is assumed that the abrasive-workpiece contact process produces small deformation, hydrostatic pressure does not cause plastic deformation, the unloading before reverse yielding is elastic unloading, and the target material is anisotropic hardened material, then the residual stress can be expressed by the following relationship

$$\sigma^r = \begin{cases} 0, & \sigma_i^e < \sigma_{y_0} \\ s^p - s^e, & \sigma_{y_0} \le \sigma_i^e \le 2\sigma_i^p \end{cases} \tag{A19}$$

This indicates that the residual stress is equal to zero during the elastic loading stage. Therefore, the residual stresses in directions x, y, and z can be expressed as

$$\begin{cases} \sigma_x{}^r = \sigma_y{}^r = \frac{1}{3}(\sigma_i^p - \sigma_i^e) \\ \sigma_z{}^r = -2\sigma_x{}^r \end{cases}, \sigma_{y_0} \le \sigma_i{}^e \le 2\sigma_i^p \tag{A20}$$

Workpiece undergoes reverse yielding and work hardening when $\sigma_i^e > 2\sigma_i^p$, as shown in Fig. A1. Elastic unloading occurs first, and the unloading stress is $2\sigma_i^p$, then reverse yielding occurs, however, there is still some stress that has not been eliminated in the process, which can be expressed as [24]

$$\Delta\sigma_i{}^e = \sigma_i{}^e - 2\sigma_i^p. \tag{A21}$$

The corresponding elastic strain can be described as

$$\Delta\varepsilon_i^e = \frac{\Delta\sigma_i^e}{E_2} \tag{A22}$$

Similar to the elastic–plastic loading process, the elastic–plastic strain can be expressed as

$$\Delta\varepsilon_i^p = \alpha\Delta\varepsilon_i^e \tag{A23}$$

The corresponding stress can be obtained as

$$\Delta\sigma_i^p = H\Delta\varepsilon_i^p \tag{A24}$$

The residual stress, when $\sigma_i^e > 2\sigma_i^p$ can be expressed as [28]

$$\begin{cases} \sigma_x{}^r = \sigma_y{}^r = \frac{1}{3}(\sigma_i^p - 2\sigma_i^p - \Delta\sigma_i^p) \\ \sigma_z{}^r = -2\sigma_x{}^r \end{cases}, \sigma_{y_0} \le \sigma_i{}^e \le 2\sigma_i^p \tag{A25}$$

Due to the number of abrasive particles from adjacent drop points is similar to each other during AWJP processing, it is reasonable to regard adjacent fields as uniform coverage. Therefore, it is assumed that the deformation field is stable and continuous, that is, ε_x, ε_y are equal to zero, and the non-zero stress and strain components will be independent of x and y directions. Therefore, it can have

$$\begin{cases} \sigma_x = \sigma_y = f(z) \\ \sigma_z = 0 \end{cases} \tag{A26}$$

$$\begin{cases} \varepsilon_x = \varepsilon_y = 0 \\ \varepsilon_z = f_1(z) \end{cases} \tag{A27}$$

However, the residual stress cannot meet the equilibrium conditions, due to the relaxation phenomenon. According to Hooke's law, the stress relaxation value can be expressed as

$$\sigma_x{}^{rel} = \sigma_y{}^{rei} = \frac{\gamma_2}{1-\gamma_2}\sigma_z \tag{A28}$$

Then, residual stress can be calculated by

$$\sigma_x{}^{fin} = \sigma_y{}^{fin} = \sigma_x{}^r - \frac{\gamma_2}{1-\gamma_2}\sigma_z{}^r = \frac{1+\gamma_2}{1-\gamma_2}\sigma_x{}^r \tag{A29}$$

The residual stress corresponding to the equivalent load P is expressed by the following relationship

$$\sigma^R = \frac{1+\gamma_2}{1-\gamma_2}\sigma_x{}^r \tag{A30}$$

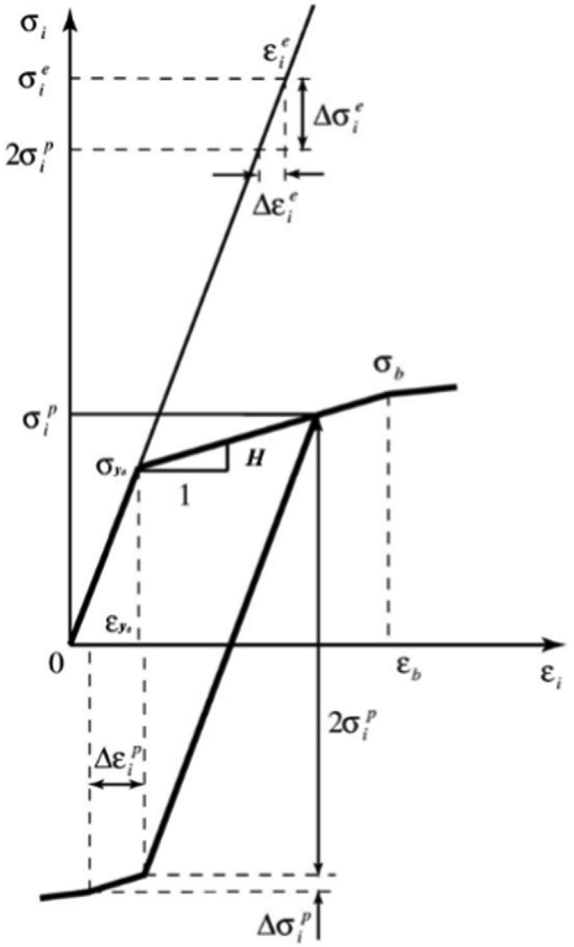

Fig. A1. Stress–strain relationship of the loading and unloading process.

References

[1] P. Lozano Torrubia, D.A. Axinte, J. Billingham, Stochastic modelling of abrasive waterjet footprints using finite element analysis, Int. J. Mach. Tools Manuf. 95 (2015) 39–51, https://doi.org/10.1016/j.ijmachtools.2015.05.001.

[2] N. Haghbin, J.K. Spelt, M. Papini, Abrasive waterjet micro-machining of channels in metals: Comparison between machining in air and submerged in water, Int. J. Mach. Tools Manuf. 88 (2015) 108–117, https://doi.org/10.1016/j.ijmachtools.2014.09.012.

[3] M.A. Azmir, A.K. Ahsan, Investigation on glass/epoxy composite surfaces machined by abrasive water jet machining, J. Mater. Process. Technol. 198 (1-3) (2008) 122–128, https://doi.org/10.1016/j.jmatprotec.2007.07.014.

[4] S. Anwar, D.A. Axinte, A.A. Becker, Finite element modelling of overlapping abrasive waterjet milled footprints, Wear 303 (1-2) (2013) 426–436, https://doi.org/10.1016/j.wear.2013.03.018.

[5] B. Sadasivam, A. Hizal, D. Arola, Abrasive waterjet peening with elastic prestress: A parametric evaluation, Int. J. Mach. Tools Manuf. 49 (2) (2009) 134–141, https://doi.org/10.1016/j.ijmachtools.2008.10.001.

[6] Z. Liao, D. Xu, G.G. Luna, D. Axinte, G. Augustinavicius, J.A. Sarasua, A. Wretland, Influence of surface integrity induced by multiple machining processes upon the fatigue performance of a nickel based superalloy, J. Mater. Process. Technol. 298 (2021) 117313, https://doi.org/10.1016/j.jmatprotec.2021.117313.

[7] D. Xu, Z. Liao, D. Axinte, M. Hardy, A novel method to continuously map the surface integrity and cutting mechanism transition in various cutting conditions, Int. J. Mach. Tools Manuf. 151 (2020) 103529, https://doi.org/10.1016/j.ijmachtools.2020.103529.

[8] X. Wang, Z. Wang, G. Wu, J. Gan, Y. Yang, H. Huang, J. He, H. Zhong, Combining the finite element method and response surface methodology for optimization of shot peening parameters, Int. J. Fatigue. 129 (2019) 105231, https://doi.org/10.1016/j.ijfatigue.2019.105231.

[9] K. Balamurugan, M. Uthayakumar, S. Gowthaman, R. Pandurangan, A study on the compressive residual stress due to waterjet cavitation peening, Eng. Fail. Anal. 92 (2018) 268–277, https://doi.org/10.1016/j.engfailanal.2018.05.012.

[10] D. Arola, M.L. McCain, S. Kunaporn, M. Ramulu, Waterjet and abrasive waterjet surface treatment of titanium: A comparison of surface texture and residual stress, Wear 249 (10-11) (2001) 943–950, https://doi.org/10.1016/S0043-1648(01)00826-2.

[11] D. Arola, C.L. Hall, Parametric effects on particle deposition in abrasive waterjet surface treatments, Mach. Sci. Technol. 8 (2) (2004) 171–192, https://doi.org/10.1081/MST-200028726.

[12] D.D. Arola, M.L. McCain, Abrasive waterjet peening: A new method of surface preparation for metal orthopedic implants, J. Biomed. Mater. Res. 53 (2000) 536–546, https://doi.org/10.1002/1097-4636(200009)53:5<536::AID-JBM13>3.0.CO;2-V.

[13] B. Sadasivam, D. Arola, An examination of abrasive waterjet peening with elastic pre-stress and the effects of boundary conditions, Mach. Sci. Technol. 16 (1) (2012) 71–95, https://doi.org/10.1080/10910344.2012.648565.

[14] M. Zhang, Z. He, Y. Zhang, X. Wang, S. Zhao, T. Fu, L. Chen, Theoretical and Finite Element Analysis of Residual Stress Field for Different Geometrical Features after Abrasive Waterjet Peening, J. Press. Vessel Technol. Trans. ASME. 141 (2019), https://doi.org/10.1115/1.4041940.

[15] Z. Liao, A. la Monaca, J. Murray, A. Speidel, D. Ushmaev, A. Clare, D. Axinte, R. M'Saoubi, Surface integrity in metal machining - Part I: Fundamentals of surface characteristics and formation mechanisms, Int. J. Mach. Tools Manuf. 162 (2021) 103687, https://doi.org/10.1016/j.ijmachtools.2020.103687.

[16] A. la Monaca, J.W. Murray, Z. Liao, A. Speidel, J.A. Robles-Linares, D.A. Axinte, M.C. Hardy, A.T. Clare, Surface integrity in metal machining - Part II: Functional performance, Int. J. Mach. Tools Manuf. 164 (2021) 103718, https://doi.org/10.1016/j.ijmachtools.2021.103718.

[17] Z. Liao, A. Abdelhafeez, H. Li, Y. Yang, O.G. Diaz, D. Axinte, State-of-the-art of surface integrity in machining of metal matrix composites, Int. J. Mach. Tools Manuf. 143 (2019) 63–91, https://doi.org/10.1016/j.ijmachtools.2019.05.006.

[18] Z. Liao, I. Sanchez, D. Xu, D. Axinte, G. Augustinavicius, A. Wretland, Dual-processing by abrasive waterjet machining—A method for machining and surface modification of nickel-based superalloy, J. Mater. Process. Technol. 285 (2020) 116768, https://doi.org/10.1016/j.jmatprotec.2020.116768.

[19] A.H. Mahmoudi, A. Ghasemi, G.H. Farrahi, K. Sherafatnia, A comprehensive experimental and numerical study on redistribution of residual stresses by shot peening, Mater. Des. 90 (2016) 478–487, https://doi.org/10.1016/j.matdes.2015.10.162.

[20] Y. Wen, Y. Wu, L. Hua, L. Xie, L. Wang, L.-C. Zhang, W. Lu, Effects of shot peening on microstructure evolution and mechanical properties of surface nanocrystal layer on titanium matrix composite, Mater. Des. 206 (2021) 109760, https://doi.org/10.1016/j.matdes.2021.109760.

[21] E. Salvati, A.J.G. Lunt, C.P. Heason, G.J. Baxter, A.M. Korsunsky, An analysis of fatigue failure mechanisms in an additively manufactured and shot peened IN 718 nickel superalloy, Mater. Des. 191 (2020) 108605, https://doi.org/10.1016/j.matdes.2020.108605.

[22] S. Bagherifard, S. Slawik, I. Fernández-Pariente, C. Pauly, F. Mücklich, M. Guagliano, Nanoscale surface modification of AISI 316L stainless steel by severe shot peening, Mater. Des. 102 (2016) 68–77, https://doi.org/10.1016/j.matdes.2016.03.162.

[23] C. Wang, C. Jiang, F. Cai, Y. Zhao, K. Zhu, Z. Chai, Effect of shot peening on the residual stresses and microstructure of tungsten cemented carbide, Mater. Des. 95 (2016) 159–164, https://doi.org/10.1016/j.matdes.2016.01.101.

[24] J.K. Li, Y. Mei, W. Duo, W. Renzhi, I / i, 147 (1991) 167–173.

[25] S. Shen, S.N. Atluri, An analytical model for shot-peening induced residual stresses, Comput. Mater. Contin. 4 (2006) 75–85, https://doi.org/10.3970/cmc.2006.004.075.

[26] A.S. Franchim, V.S.d. Campos, D.N. Travessa, C.d.M. Neto, Analytical modelling for residual stresses produced by shot peening, Mater. Des. 30 (5) (2009) 1556–1560, https://doi.org/10.1016/j.matdes.2008.07.040.

[27] H.Y. Miao, S. Larose, C. Perron, M. Lévesque, An analytical approach to relate shot peening parameters to Almen intensity, Surf. Coatings Technol. 205 (7) (2010) 2055–2066, https://doi.org/10.1016/j.surfcoat.2010.08.105.

[28] K. Sherafatnia, G.H. Farrahi, A.H. Mahmoudi, A. Ghasemi, Experimental measurement and analytical determination of shot peening residual stresses considering friction and real unloading behavior, Mater. Sci. Eng. A. 657 (2016) 309–321, https://doi.org/10.1016/j.msea.2016.01.070.

[29] Y.F. Al-Obaid, Shot peening mechanics: experimental and theoretical analysis, Mech. Mater. 19 (2-3) (1995) 251–260, https://doi.org/10.1016/0167-6636(94)00036-G.

[30] R. Fathallah, G. Inglebert, L. Castex, Prediction of plastic deformation and residual stresses induced in metallic parts by shot peening, Mater. Sci. Technol. 14 (7) (1998) 631–639, https://doi.org/10.1179/mst.1998.14.7.631.

[31] S. Kunaporn, M. Ramulu, M. Hashish, Mathematical modeling of ultra-high-pressure waterjet peening, J. Eng. Mater. Technol. Trans. ASME. 127 (2005) 186–191, https://doi.org/10.1115/1.1857934.

[32] R. Balz, K.C. Heiniger, Determination of Spatial Velocity Distributions of Abrasive Particles in Abrasive Water Jets Using Laser-Induced Fluorescence Under Real Conditions, WJTA-IMCA Conf. Expo. (2011).

[33] D.A. Axinte, B. Karpuschewski, M.C. Kong, A.T. Beaucamp, S. Anwar, D. Miller, M. Petzel, High Energy Fluid Jet Machining (HEFJet-Mach): From scientific and technological advances to niche industrial applications, CIRP Ann. - Manuf. Technol. 63 (2) (2014) 751–771, https://doi.org/10.1016/j.cirp.2014.05.001.

[34] M. Mieszala, P.L. Torrubia, D.A. Axinte, J.J. Schwiedrzik, Y. Guo, S. Mischler, J. Michler, L. Philippe, Erosion mechanisms during abrasive waterjet machining: Model microstructures and single particle experiments, J. Mater. Process. Technol. 247 (2017) 92–102, https://doi.org/10.1016/j.jmatprotec.2017.04.003.

[35] R. Balz, R. Mokso, C. Narayanan, D.A. Weiss, K.C. Heiniger, Ultra-fast X-ray particle velocimetry measurements within an abrasive water jet, Exp. Fluids. 54 (3) (2013), https://doi.org/10.1007/s00348-013-1476-8.

[36] P. Debusk, R. Kruger, D. Weber, J. Wolgamott, L. Loper, WaterJet Technology Association 2003 WJTA Conference Committee WJTA Administration, (2003).

[37] H.J. Kleemola, M.A. Nieminen, on the Strain-Hardening Parameters of Metals, Met. Trans. 5 (8) (1974) 1863–1866, https://doi.org/10.1007/BF02644152.

[38] Z. Wang, H.N. Li, T.B. Yu, H. Chen, J. Zhao, On the predictive modelling of machined surface topography in abrasive air jet polishing of quartz glass, Int. J. Mech. Sci. 152 (2019) 1–18, https://doi.org/10.1016/j.ijmecsci.2018.12.041.

[39] Z. Wang, H. Nan Li, T.B. Yu, Z.X. Wang, J. Zhao, Analytical model of dynamic and overlapped footprints in abrasive air jet polishing of optical glass, Int. J. Mach. Tools Manuf. 141 (2019) 59–77, https://doi.org/10.1016/j.ijmachtools.2019.03.005.

[40] X-ray Diffraction Residual Stress Measurement: An Introduction, Www. Protoxrd.Com. (2011).

[41] Z. Yang, L. Zhu, G. Zhang, C. Ni, B. Lin, Review of ultrasonic vibration-assisted machining in advanced materials, Int. J. Mach. Tools Manuf. 156 (2020) 103594, https://doi.org/10.1016/j.ijmachtools.2020.103594.

[42] M. Algarni, Y. Bai, Y. Choi, A study of Inconel 718 dependency on stress triaxiality and Lode angle in plastic deformation and ductile fracture, Eng. Fract. Mech. 147 (2015) 140–157, https://doi.org/10.1016/j.engfracmech.2015.08.007.

[43] W.-S. Lee, C.-F. Lin, T.-H. Chen, H.-W. Chen, Dynamic mechanical behaviour and dislocation substructure evolution of Inconel 718 over wide temperature range, Mater. Sci. Eng. A. 528 (19-20) (2011) 6279–6286, https://doi.org/10.1016/j.msea.2011.04.079.

[44] J. Wu, H. Liu, P. Wei, Q. Lin, S. Zhou, Effect of shot peening coverage on residual stress and surface roughness of 18CrNiMo7-6 steel, Int. J. Mech. Sci. 183 (2020) 105785, https://doi.org/10.1016/j.ijmecsci.2020.105785.

[45] J. Wu, H. Liu, P. Wei, C. Zhu, Q. Lin, Effect of shot peening coverage on hardness, residual stress and surface morphology of carburized rollers, Surf. Coatings Technol. 384 (2020) 125273, https://doi.org/10.1016/j.surfcoat.2019.125273.